Toward spectral engineering of squeezed light in high-gain parametric down-conversion

Jatin Kumar,[1,*] Aleksa Krstić,[1] Sina Saravi,[1,2,3,4] and Frank Setzpfandt[1,5]

[1]*Institute of Applied Physics, Abbe Center of Photonics, Friedrich Schiller University Jena, Albert-Einstein-Straße 15, 07745 Jena, Germany*

[2]*Heinz Nixdorf Institute, Paderborn University, Fürstenallee 11, 33102 Paderborn, Germany*

[3]*Department of Electrical Engineering and Information Technology, Paderborn University, Warburger Straße 100, 33098 Paderborn, Germany*

[4]*Institute for Photonic Quantum Systems, Paderborn University, Warburger Straße 100, 33098 Paderborn, Germany*

[5]*Fraunhofer Institute for Applied Optics and Precision Engineering, Albert-Einstein-Straße 7, 07745 Jena, Germany*

(Received 15 January 2026; revised 25 June 2026; accepted 17 July 2026; published 10 August 2026)

We investigated the spectral properties of squeezed light generated via parametric down-conversion in the high-gain regime, considering both unapodized and apodized dispersion-engineered waveguides. The gain-dependent evolution of these states is examined starting from the low-gain regime, which includes both highly correlated and nearly uncorrelated cases. For the unapodized configuration, our simulated results show a monotonic increase in spectral purity with gain, whereas for some of the apodized configuration, they exhibit a nonmonotonic dependence, initially decreasing and then recovering at higher gain. By combining Schmidt-mode analysis with a group-velocity-based interpretation, we explain why different dispersion conditions exhibit distinct gain-dependent behavior, specifically that rapid purification occurs when the pump group velocity lies between those of the signal and idler. Our study shows that the evolution of spectral purity is governed primarily by the underlying dispersion of the waveguide. These results demonstrate that dispersion engineering and parametric gain can be jointly exploited to tailor the spectral-mode structure of squeezed-light sources, enabling their optimization for a broad range of quantum applications.

DOI: 10.1103/2hth-yy33

I. INTRODUCTION

Squeezed light has in recent years become a cornerstone resource in modern quantum technologies, enabling advances in computing, communication, imaging, and metrology [1–4]. In quantum computing, squeezed states form the basis of continuous-variable quantum information processing [5,6] and have been used in Gaussian boson sampling to demonstrate quantum computational advantage [7–9]. In quantum communication, they facilitate secure protocols such as continuous-variable quantum key distribution [10–12]. In the domain of quantum imaging, squeezed light improves resolution and sensitivity beyond the classical shot-noise limit, allowing techniques like subdiffraction imaging and phase-contrast microscopy [13–15]. Finally, in quantum metrology, squeezed states enhance precision by reducing quantum noise in interferometric measurements [16,17], most notably improving the sensitivity of gravitational wave detectors such as LIGO via squeezed vacuum injection [18].

Squeezed light is predominantly generated via nonlinear optical processes [19–21], with parametric down-conversion (PDC) being a widely employed technique [22]. In PDC, pump photons propagating through a $\chi^{(2)}$ nonlinear medium are converted into pairs of signal and idler photons. This process obeys the laws of energy and momentum conservation, leading to quantum correlations between the resulting signal and idler photons [23]. At sufficiently low pump intensities, mainly signal and idler photon pairs are generated, and the PDC source is said to operate in the low-gain regime. In contrast, when a high-intensity pump is used, the generated photon pairs can further stimulate down-conversion events, leading to an exponential increase in photon production; this regime is known as the high-gain regime [24]. Under these conditions, the quantum correlations of individual photon pairs collectively give rise to strong squeezing [25,26].

For practical applications, precise control over the spectral, temporal, and statistical properties of squeezed light is crucial [27–29]. The advent of integrated photonics platforms has opened new possibilities to control these properties to a very high degree [30]. In particular, waveguides (WGs) can be engineered to precisely control effective indices, group velocities, and phase-matching conditions [31–34], thereby tailoring the spectral and temporal properties of the generated quantum fields. As a result, integrated WG platforms have emerged as ideal sources for the generation of quantum light, offering enhanced scalability, stability, and control [35,36]. In this context, understanding the evolution of spectral correlations in the high-gain regime across different nonlinear platforms is essential. In $\chi^{(3)}$-based platforms, parametric processes such as four-wave mixing have been used to control the

*Contact author: jatin.kumar@uni-jena.de

Published by the American Physical Society under the terms of the Creative Commons Attribution 4.0 International license. Further distribution of this work must maintain attribution to the author(s) and the published article's title, journal citation, and DOI.

spectral correlations and temporal-mode structure of squeezed states through the interplay of dispersion engineering, pump shaping, Kerr nonlinearities, and parametric gain [37–42]. Thus, at the level of the generated quantum state, both PDC in $\chi^{(2)}$ media and four-wave mixing in $\chi^{(3)}$ media provide routes to engineer spectral correlations. In the present work, we focus on $\chi^{(2)}$-based systems. In $\chi^{(2)}$ WGs, both single-pass and cavity-enhanced geometries are possible. However, cavity-enhanced systems impose discrete resonant modes and feedback, favoring narrowband operation and limiting access to broadband spectral correlations [43–46]. In contrast, single-pass $\chi^{(2)}$ WGs operate in a regime where the modal structure is governed directly by dispersion, enabling systematic and predictive spectral engineering through gain-dependent evolution.

Among integrated $\chi^{(2)}$ platforms, lithium niobate on insulator (LNOI) is an exceptionally suitable platform for integrated quantum photonics due to its strong $\chi^{(2)}$ nonlinearity, tight modal confinement, low propagation loss, and flexible dispersion engineering [35,47,48]. In addition, the efficiency of nonlinear interactions can be further enhanced via poling [49]. Several experimental demonstrations on LNOI-based platforms have successfully generated squeezed light, including broadband squeezed vacuum generation [50], squeezing at telecom wavelengths [51], and quadrature squeezed light in integrated nanophotonic WGs [45].

When designing a high-gain source, in addition to the aforementioned platform-specific techniques, special care must be taken to account for the effects that high-gain operation has on the spectral, temporal, and statistical properties of the output light. These effects include spectral broadening, changes in spectral purity, temporal reshaping, and photon bunching, each of which can significantly impact the performance of quantum applications [52–55]. Understanding these high-gain effects is therefore crucial for optimizing source performance in practical implementations.

In this work our goal is to understand how the spectral correlations in the output state of a WG-based PDC source are affected by increasing gain and whether certain types of low-gain correlations lead to more favorable spectral properties in the high-gain regime. More broadly, we aim to clarify, in principle, how different low-gain spectral configurations behave under high-gain conditions and what implications they carry for the engineering of quantum light sources tailored to specific application demands. From this analysis, we identify the relative group-velocity ordering of the pump, signal, and idler as the key parameter that determines whether the generated squeezed light undergoes slow, accelerated, or nonmonotonic spectral purification, thereby providing clear dispersion-engineering design principles for controlling the spectral correlations of the output state.

In this paper we employ a theoretical formalism for high-gain PDC in WGs that accommodates arbitrary dispersion relations. This framework is particularly well suited for modeling modern integrated platforms, such as LNOI, where complex dispersion can be harnessed to engineer quantum state generation [56,57]. We investigate the key WG parameters that control the spectral properties of the generated squeezed light. Specifically, we focus on three sets of dispersion conditions to study the behavior of gain and spectral purity for apodized and unapodized phase-matching scenarios. In Sec. II the theoretical formalism is discussed. In Sec. III we investigate high-gain PDC through numerical simulations and analyze its gain-dependent spectral behavior. Section IV summarizes our work and discusses our findings.

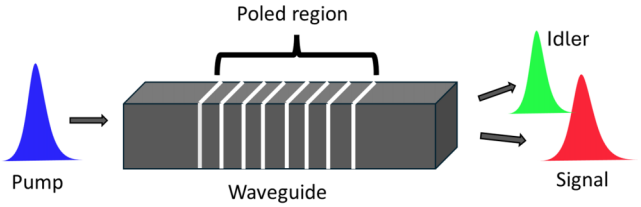


FIG. 1. Schematic of the PDC process in a WG where the pump interacts with the nonlinear medium of the WG to generate signal and idler fields.

II. THEORY

The theoretical description of nonlinear light-matter interactions depends strongly on how dispersion is treated. In many works, a weak-dispersion approximation is used, where the temporal degree of freedom is replaced by a spatial one [58,59]. In this work we adopt a time-domain approach that accurately accounts for arbitrary dispersion. This more general formalism enables us to capture complex dispersion effects that can arise in WGs engineered with nanostructuring or other intricate geometrical features [60,61].

Here we consider a nonlinear WG with a pulsed pump to generate two-mode squeezed light, where the signal and idler modes are distinct guided modes and all modes propagate in the same direction. The WG is assumed to be infinitely extended along the z axis, with a finite poled region of length L, as illustrated in Fig. 1. The transverse geometry, together with the dielectric permittivity distribution, determines the linear characteristics of the guided modes, specifically their effective indices, group velocities, and transverse mode profiles.

For the aforementioned WG, assuming that material dispersion is negligible, the quantized electric field for the signal and idler modes (positive-frequency part) is defined as [62,63]

$$\hat{\mathbf{E}}^{j(+)}(\mathbf{r},t) = i\gamma \int \mathrm{d}\omega \sqrt{\frac{\omega n_g^j(\omega)}{N_j(\omega)}} \mathbf{E}^j(x,y,\omega) \times \exp i[k_j(\omega)z]\hat{c}_\omega^j(t), \quad j \in \{s,i\}, \tag{1}$$

where $j = s$ corresponds to the signal mode, $j = i$ corresponds to the idler mode, $\gamma = \sqrt{\frac{\hbar}{4\pi\varepsilon_0 c}}$, $\mathbf{E}^j(x,y,\omega)$ is the transverse mode profile, $n_g^j(\omega)$ is the modal group index, and $N_j(\omega) = \iint \mathrm{d}x\,\mathrm{d}y\,\varepsilon_r(x,y,\omega)|\mathbf{E}^j(x,y,\omega)|^2$ is a mode normalization constant. Here, $\hat{c}_\omega^s(t) \equiv \hat{a}_\omega(t)$ and $\hat{c}_\omega^i(t) \equiv \hat{b}_\omega(t)$ are the annihilation operators for the signal and idler modes, respectively. The annihilation operators $\hat{c}_\omega^j(t)$ and creation operators $\hat{c}_\omega^{j'\dagger}(t)$ obey the canonical commutation relation $[\hat{c}_\omega^j(t), \hat{c}_{\omega'}^{j'\dagger}(t)] = \delta_{jj'}\delta(\omega-\omega')$.

In this work we employ the Heisenberg picture. In addition, throughout the paper, spatial integrals are taken over the transverse cross-sectional area A and along the longitudinal axis of the WG over the domain $z \in [0, L]$, frequency integrals

are taken over the interval $[0, \infty)$, and time-domain integrals extend over $(-\infty, \infty)$.

To describe the PDC process, we consider the following form of the nonlinear interaction Hamiltonian [63]:

$$\hat{H}_{\mathrm{PDC}}(t) = -2\varepsilon_0 \int \mathrm{d}^3\mathbf{r}\, \chi^{(2)}_{ljm}(\mathbf{r}) E_l^{p(+)}(\mathbf{r}, t) \hat{E}_j^{s(-)}(\mathbf{r}, t) \times \hat{E}_m^{i(-)}(\mathbf{r}, t) + \mathrm{H.c.} \tag{2}$$

Here ε_0 is the vacuum permittivity, $\chi^{(2)}_{ljm}$ is the second-order nonlinear susceptibility tensor, $E_l^{p(+)}(\mathbf{r}, t)$ is the positive-frequency component of the pump field, $\hat{E}_j^{s(-)}(\mathbf{r}, t)$ is the negative-frequency component of the signal field, $\hat{E}_m^{i(-)}(\mathbf{r}, t)$ is the negative-frequency component of the idler field, and H.c. denotes the Hermitian conjugate. To drive the nonlinear interaction in the WG, we assume a classical undepleted pump pulse with a Gaussian temporal envelope.

The Gaussian pump pulse is defined as

$$\mathbf{E}^{p(+)}(\mathbf{r}, t) = \gamma_p \int \mathrm{d}\omega_p \sqrt{\frac{n_g^p(\omega_{p_0})}{N_p(\omega_p)}} \alpha(\omega_p) \mathbf{E}^p(x, y, \omega_p) \times \exp i[k_p(\omega_p) z - \omega_p t], \tag{3}$$

where $\gamma_p = \sqrt{\frac{P_p}{4\pi\varepsilon_0 c \sigma_p^2}}$ incorporates the pump peak power P_p, speed of light c, and vacuum permittivity ε_0. The group index is denoted by n_g^p. The function $\alpha(\omega_p) = \exp(-\frac{(\omega_p - \omega_{p_0})^2}{2\sigma_p^2})$ represents the Gaussian spectral envelope centered at ω_{p_0} with bandwidth σ_p. Here, $\mathbf{E}^p(x, y, \omega_p)$ is the transverse field profile of the pump and $N_p(\omega_p) = \iint \mathrm{d}x\, \mathrm{d}y\, \varepsilon_r(x, y, \omega_p) |\mathbf{E}^p(x, y, \omega_p)|^2$ is the normalization constant for the transverse pump mode profile with relative permittivity ε_r.

Since we are working in the Heisenberg picture, the total Hamiltonian of the system includes the free (time-independent) part H_0 and the nonlinear interaction part $H_{\mathrm{PDC}}(t)$. The free Hamiltonian is

$$H_0 = \sum_{j=s,i} \int \mathrm{d}\omega_j \hbar\omega_j \hat{c}_\omega^{j\dagger}(t) \hat{c}_\omega^j(t), \tag{4}$$

which governs the free evolution of each mode. To remove this trivial evolution we transform to a rotating frame by

$$\hat{c}_\omega^j(t) = \tilde{c}_\omega^j(t) e^{-i\omega t}, \quad j \in \{s, i\},$$

where $\tilde{c}_\omega^j(t)$ are slowly varying operators that evolve only due to the nonlinear interaction [64,65]. With this transformation, the Heisenberg equation of motion for the slowly varying operators becomes

$$i\hbar \partial_t \tilde{c}_\omega^j(t) = \left[\tilde{c}_\omega^j(t), H_{\mathrm{PDC}}(t)\right]. \tag{5}$$

Applying this to the slowly varying signal and idler operators $\tilde{a}_{\omega_s'}(t)$ and $\tilde{b}_{\omega_i'}(t)$, we obtain coupled integrodifferential equations among the creation and annihilation operators

$$\begin{aligned} \partial_t \tilde{a}_{\omega_s'}(t) &= -\frac{i}{\hbar} \int \mathrm{d}\omega_i G_1(\omega_i, \omega_s', t) \tilde{b}_{\omega_i}^\dagger, \\ \partial_t \tilde{b}_{\omega_i'}(t) &= -\frac{i}{\hbar} \int \mathrm{d}\omega_s G_2(\omega_s, \omega_i', t) \tilde{a}_{\omega_s}^\dagger. \end{aligned} \tag{6}$$

These coupled integrodifferential equations involve the kernels $G_1(\omega_i, \omega_s', t)$ and $G_2(\omega_s, \omega_i', t)$, which represent the nonlinear coupling between the modes. The kernels $G_1(\omega_i, \omega_s', t)$ and $G_2(\omega_s, \omega_i', t)$ are defined as

$$G_1(\omega_i, \omega_s', t) = M \frac{\hbar\gamma_p}{2\pi c} \sqrt{\omega_s' \omega_i n_g^p(\omega_{p_0}) n_g^s(\omega_s') n_g^i(\omega_i)} \int \mathrm{d}\omega_p \alpha(\omega_p) \phi(\omega_i, \omega_s', \omega_p) \exp[-i(\omega_p - \omega_i - \omega_s')t], \tag{7}$$

$$G_2(\omega_s, \omega_i', t) = M \frac{\hbar\gamma_p}{2\pi c} \sqrt{\omega_i' \omega_s n_g^p(\omega_{p_0}) n_g^i(\omega_i') n_g^s(\omega_s)} \int \mathrm{d}\omega_p \alpha(\omega_p) \phi(\omega_s, \omega_i', \omega_p) \exp[-i(\omega_p - \omega_s - \omega_i')t]. \tag{8}$$

The key factors in the coupling kernels are the phase-matching function $\phi(\omega_i, \omega_s, \omega_p)$ and the nonlinear mode-overlap factor M. The phase-matching function is defined as

$$\phi(\omega_i, \omega_s, \omega_p) = \int \mathrm{d}z\, f(z) \exp[i\Delta k(\omega_i, \omega_s, \omega_p) z], \tag{9}$$

where $f(z)$ represents the spatial modulation of the nonlinearity along the propagation direction, determined by the poling profile of the WG (see Appendix B for details). The phase mismatch between the interacting modes is defined as

$$\Delta k(\omega_i, \omega_s, \omega_p) = k_p(\omega_p) - k_s(\omega_s) - k_i(\omega_i). \tag{10}$$

Here $k_p(\omega_p)$, $k_s(\omega_s)$, and $k_i(\omega_i)$ are the propagation constants of the pump, signal, and idler modes, respectively. The nonlinear mode-overlap factor M is given by

$$M = \int \mathrm{d}x\, \mathrm{d}y \frac{\chi^{(2)}_{ljm}}{\sqrt{N_p N_s N_i}} E_l^p(x, y, \omega_p) E_j^{s*}(x, y, \omega_s) \times E_m^{i*}(x, y, \omega_i) \tag{11}$$

and is evaluated under the assumption that the transverse mode profiles remain effectively constant over the frequency range of interest.

Since the PDC Hamiltonian is quadratic in the creation and annihilation operators, we can use a Bogoliubov transformation to describe the evolution of the operators [66]. This transformation, also known as the input-output transformation, is a standard theoretical tool for describing high-gain PDC [63,67]. Here the input operators correspond to the initial time and the output operators correspond to the final time. The input-output relations for $\tilde{a}_{\omega_s}(t)$ and $\tilde{b}_{\omega_i}(t)$ are expressed as

$$\tilde{a}_{\omega_s}(t) = \int \mathrm{d}\omega_s'' A(\omega_s, \omega_s'', t) \tilde{a}_{\omega_s''}(t_0) + \int \mathrm{d}\omega_i'' B(\omega_s, \omega_i'', t) \tilde{b}_{\omega_i''}^\dagger(t_0), \tag{12}$$

$$\tilde{b}_{\omega_i}(t) = \int \mathrm{d}\omega_i'' C(\omega_i, \omega_i'', t)\tilde{b}_{\omega_i''}(t_0) + \int \mathrm{d}\omega_s'' D(\omega_i, \omega_s'', t)\tilde{a}^{\dagger}_{\omega_s''}(t_0), \quad (13)$$

where $A(\omega_s, \omega_s'', t)$, $B(\omega_s, \omega_i'', t)$, $C(\omega_i, \omega_i'', t)$, and $D(\omega_i, \omega_s'', t)$ are complex-valued scalar functions that relate the input and output operators. To ensure that the Bogoliubov transformation preserves the canonical commutation relations, the complex-valued scalar functions must satisfy specific constraints. These constraints provide a necessary consistency check of the formalism and are

$$[\tilde{a}_{\omega_s}(t), \tilde{a}^{\dagger}_{\omega_s'}(t)] = \int \mathrm{d}\omega_s'' A(\omega_s, \omega_s'', t)A^*(\omega_s', \omega_s'', t) - \int \mathrm{d}\omega_i'' B(\omega_s, \omega_i'', t)B^*(\omega_s', \omega_i'', t) = \delta(\omega_s - \omega_s'), \quad (14)$$

$$[\tilde{b}_{\omega_i}(t), \tilde{b}^{\dagger}_{\omega_i'}(t)] = \int \mathrm{d}\omega_i'' C(\omega_i, \omega_i'', t)C^*(\omega_i', \omega_i'', t) - \int \mathrm{d}\omega_s'' D(\omega_i, \omega_s'', t)D^*(\omega_i', \omega_s'', t) = \delta(\omega_i - \omega_i'), \quad (15)$$

$$[\tilde{a}_{\omega_s}(t), \tilde{b}_{\omega_i}(t)] = \int \mathrm{d}\omega_s'' A(\omega_s, \omega_s'', t)D(\omega_i, \omega_s'', t) - \int \mathrm{d}\omega_i'' B(\omega_s, \omega_i'', t)C(\omega_i, \omega_i'', t) = 0. \quad (16)$$

Substituting Eqs. (12) and (13) into Eq. (6), we obtain a set of coupled integrodifferential equations expressed in terms of complex scalar functions. With the infusion of the Bogoliubov transformation in the operator formalism, the description transitions to a scalar formalism, which is easier to handle and allows us to work directly with these complex-valued functions A, B, C, and D. The resulting coupled integrodifferential equations are given by

$$\begin{aligned}
\partial_t A(\omega_s', \omega_s'', t) &= -\frac{i}{\hbar}\int \mathrm{d}\omega_i G_1(\omega_i, \omega_s', t)D^*(\omega_i, \omega_s'', t),\\
\partial_t B(\omega_s', \omega_i'', t) &= -\frac{i}{\hbar}\int \mathrm{d}\omega_i G_1(\omega_i, \omega_s', t)C^*(\omega_i, \omega_i'', t),\\
\partial_t C(\omega_i', \omega_i'', t) &= -\frac{i}{\hbar}\int \mathrm{d}\omega_s G_2(\omega_s, \omega_i', t)B^*(\omega_s, \omega_i'', t),\\
\partial_t D(\omega_i', \omega_s'', t) &= -\frac{i}{\hbar}\int \mathrm{d}\omega_s G_2(\omega_s, \omega_i', t)A^*(\omega_s, \omega_s'', t). \quad (17)
\end{aligned}$$

Since all the field properties are embedded in the complex functions, we study the properties of the squeezed state by solving the resulting coupled integrodifferential equations. We solve these equations numerically by incorporating the initial conditions

$$\begin{aligned}
A(\omega_s', \omega_s'', t_0) &= \delta(\omega_s' - \omega_s''),\\
C(\omega_i', \omega_i'', t_0) &= \delta(\omega_i' - \omega_i''),\\
D(\omega_i', \omega_s'', t_0) &= 0,\\
B(\omega_s', \omega_i'', t_0) &= 0. \quad (18)
\end{aligned}$$

These initial conditions are determined from Eqs. (12) and (13) evaluated at time t_0.

Since squeezed states belong to the class of Gaussian states, which are fully characterized by their first- and second-order moments [68], the output quantum state produced by the nonlinear WG can be completely described using these moments. In our case, the first-order moments of the form $\langle\tilde{a}^{(\dagger)}_{\omega}(t)\rangle$ and $\langle\tilde{b}^{(\dagger)}_{\omega}(t)\rangle$ vanish, so only the second-order moments need to be calculated, which are given by

$$\langle 0|\tilde{a}_{\omega_s}(t)\tilde{b}_{\omega_i}(t)|0\rangle = \int \mathrm{d}\omega_s'' A(\omega_s, \omega_s'', t)D(\omega_i, \omega_s'', t). \quad (19)$$

To investigate the spectral properties of the output quantum state, we further decompose the second-order moments defined in Eq. (19) in terms of the Schmidt modes. These modes are obtained via the singular value decomposition of the scalar functions from Eqs. (12) and (13) [53]. The Schmidt-mode decomposition provides a clear interpretation of the multimode structure of squeezed light in the spectral domain. It offers an intuitive physical picture where each mode corresponds to a distinct wave packet [69], allowing the signal and idler beams to be described as superpositions of these modes. In terms of the Schmidt modes, the second-order moments are expressed as [59]

$$\langle 0|\tilde{a}_{\omega_s}(t)\tilde{b}_{\omega_i}(t)|0\rangle = \sum_{\ell}\frac{\sinh(2r^{(\ell)})}{2}\psi_s^{(\ell)}(\omega_s)\psi_i^{(\ell)}(\omega_i), \quad (20)$$

where the Schmidt modes, denoted by $\psi^{(\ell)}_{s\,(i)}$ for the signal (idler), form an orthonormal basis. Each pair of modes ℓ is associated with a squeezing parameter $r^{(\ell)}$, which quantifies the squeezing strength in that mode. From the second-order moment in Eq. (20), expressed in terms of Schmidt modes, we can reconstruct the joint spectral amplitude (JSA). The JSA is given by

$$\mathcal{J}(\omega_s, \omega_i) = \sum_{\ell} r^{(\ell)}\psi_s^{(\ell)}(\omega_s)\psi_i^{(\ell)}(\omega_i). \quad (21)$$

In the low-gain regime, where $r^{(\ell)} \ll 1$, the second-order moment in Eq. (20) converges to the JSA, so no reconstruction is needed. However, at high gain (large $r^{(\ell)}$) the second-order moment no longer directly represents the JSA, and explicit reconstruction is required.

Since our goal is to characterize the spectral properties of squeezed states relevant for practical applications, the spectral purity provides a physically meaningful figure of merit. To evaluate it, we extract the squeezing parameters $r^{(\ell)}$ from Eq. (20), which encodes the Schmidt-mode structure of the state. The spectral purity $\mathcal{P}$ is defined as [59]

$$\mathcal{P} = \frac{\sum_{\ell}\sinh^4(r^{(\ell)})}{[\sum_{\ell}\sinh^2(r^{(\ell)})]^2}. \quad (22)$$

It provides a quantitative measure of the multimode character of the squeezed state, with $\mathcal{P} = 1$ corresponding to an ideal single-mode squeezed state.

In addition, the extracted squeezing parameters $r^{(\ell)}$ quantify the overall strength of the parametric process. Following

Ref. [53], we define an overall parametric gain G as

$$G = \sqrt{\sum_{\ell} (r^{(\ell)})^2}. \tag{23}$$

The corresponding gain expressed in decibels is given by

$$G_{\mathrm{dB}} = -10 \log_{10}(e^{-2G}). \tag{24}$$

Finally, to study the gain-dependent behavior of the Schmidt modes, we perform a mode-contribution analysis. For this purpose, we introduce the normalized modal weights p_ℓ, defined as

$$p_\ell = \frac{\sinh^2(r^{(\ell)})}{\sum_\ell \sinh^2(r^{(\ell)})}, \quad \sum_\ell p_\ell = 1. \tag{25}$$

These weights quantify the fractional photon-pair population associated with the ℓth Schmidt-mode pair [59]. Correspondingly, the spectral purity in Eq. (22) can equivalently be expressed as $\mathcal{P} = \sum_\ell p_\ell^2$.

III. SIMULATION

In this section we investigate how increasing gain influences the spectral properties of two-mode squeezed state. To address this, we numerically solve the theoretical model presented in the preceding section.

At low gain, the JSA can be found analytically by perturbatively expanding Eq. (17). The full derivation can be found in Appendix A. It is given by the product of the pump envelope and the phase-matching function

$$J(\omega_s, \omega_i) = \alpha(\omega_s + \omega_i)\phi(\Delta k(\omega_s, \omega_i)), \tag{26}$$

where $\phi(\Delta k(\omega_s, \omega_i))$ is the phase-matching function, $\alpha(\omega_s + \omega_i)$ is the pump envelope, and $\Delta k(\omega_s, \omega_i)$ is the phase mismatch. The shape and orientation of the JSA in the (ω_s, ω_i) space is strongly influenced by the phase-matching function, which is in turn determined by the group velocities of the interacting fields. Although our formalism accounts for strong dispersion, for the present analysis, we will focus on a simplified case in which the interacting fields are considered to be sufficiently narrowband to allow a linear expansion of the dispersion relations of the involved modes. This will allow a clear geometric interpretation of the frequency correlations of the output state and enable us to focus on the underlying physical insights. Under the aforementioned assumption, it is justified to expand the phase mismatch $\Delta k(\omega_s, \omega_i)$ around the central phase-matched signal and idler frequencies [70]. Thus, we obtain

$$\Delta k(\omega_s, \omega_i) \approx \left(\frac{1}{v_g^s} - \frac{1}{v_g^p}\right)(\omega_s - \omega_{s0}) + \left(\frac{1}{v_g^i} - \frac{1}{v_g^p}\right)(\omega_i - \omega_{i0}), \tag{27}$$

where v_g^p, v_g^s, and v_g^i are the group velocities for the pump, signal, and idler modes, respectively.

To systematically study the gain-dependent effects on the spectral properties, we investigate different group-velocity combinations in the WG, which result in varied phase-matching slopes. We characterize these slopes in terms of an angle θ, defined with respect to the ω_s axis in the (ω_s, ω_i) plane [71]. The angle θ is expressed in terms of the group velocities of the pump, signal, and idler modes in the PDC process as

$$\theta = \arctan\left[-\left(\frac{v_g^s - v_g^p}{v_g^i - v_g^p}\right)\frac{v_g^i}{v_g^s}\right]. \tag{28}$$

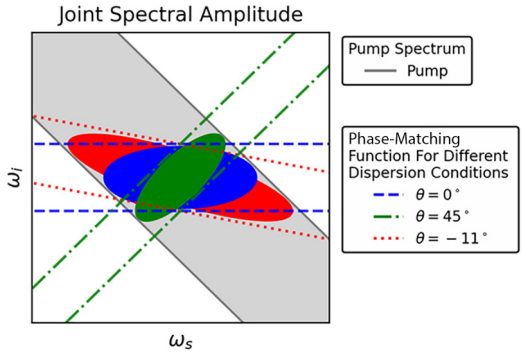


FIG. 2. Illustration of the three dispersion conditions under consideration, characterized by their respective angles θ with respect to the frequency ω_s axis. These dispersion conditions determine the phase-matching characteristics of the system and thereby the shape and orientation of the JSA at low gain [Eq. (26)]. The gray region represents the pump envelope, where the width of this region is determined by the spectral bandwidth of the pump pulse. Note that these schematics are not exact numerical JSAs but serve as visual intuition to show the initial states that form the basis for our simulations.

We consider three dispersion conditions for a fixed pump bandwidth, as illustrated in Fig. 2. The figure schematically depicts the low-gain JSAs corresponding to phase-matching angles $\theta = 0°$, $45°$, and $-11°$. At low gain, these correspond to different types of spectral correlations: One case yields a nearly uncorrelated spectrum, another produces a strongly correlated spectrum, and the third represents an intermediate situation. Specifically, the three cases correspond to distinct group-velocity relations. (i) For $\theta = 0°$, the pump and signal modes have the same group velocity, while the idler mode can in general be faster or slower than both. In our case, the idler mode group velocity is higher than that of the pump and signal modes. (ii) For $\theta = 45°$, the pump mode group velocity lies midway between those of the signal and idler modes. (iii) For $\theta = -11°$, the idler mode has a higher group velocity than the signal mode, and the signal mode has a higher group velocity than the pump mode.

To study the gain-dependent effects of different dispersion conditions, we perform numerical simulations. Since our primary objective is to investigate the gain-dependent behavior of the spectrum, we introduce certain simplifications. In particular, all linear optical properties of the WG are assumed to be identical across the different dispersion configurations, except for the group velocity of the signal mode, which is varied to modify the relative group-velocity ordering. Here, the nonlinear overlap integral defined in Eq. (11) is kept fixed at a realistic value of order 10^{-6} V^{-1} for all cases considered. This

TABLE I. Group velocities and parameters for different dispersion conditions.

Dispersion condition θ	Waveguide length L (mm)	Group-velocity pump v_g^p (m/s)	Group-velocity signal v_g^s (m/s)	Group-velocity idler v_g^i (m/s)
0°	2.5	$\frac{c}{2.168}$	$\frac{c}{2.168}$	$\frac{c}{1.909}$
45°	1.66	$\frac{c}{2.168}$	$\frac{c}{2.426}$	$\frac{c}{1.909}$
-11°	2.5	$\frac{c}{2.168}$	$\frac{c}{2.118}$	$\frac{c}{1.909}$

value is obtained by assuming constant transverse fields over an effective mode area $A_{\text{eff}} = 1\ \mu\text{m}^2$ and using the dominant lithium niobate nonlinear coefficient $\chi^{(2)}_{333} = 2d_{33}$.

To systematize the simulations, we ensure that the phase-matching bandwidth remains nearly identical across all dispersion conditions by adjusting the WG length accordingly, as it is a key parameter governing the phase-matching bandwidth. Similarly, the spectral bandwidth of the pump is kept constant across different dispersion scenarios. However, for each case, we consider both a narrowband ($\frac{\sigma_p}{\omega_{p_0}} = 0.0015$, $\sigma_t = 274.10$ fs) and a broadband ($\frac{\sigma_p}{\omega_{p_0}} = 0.003$, $\sigma_t = 137.05$ fs) pump, where $\omega_{p_0} = 2.43 \times 10^{15}\ \text{s}^{-1}$, in order to also investigate how the pump bandwidth influences the gain-dependent dynamics of the PDC spectrum. Here, to vary the nonlinear interaction strength, the pump peak power is treated as an input parameter that controls the parametric gain, which is obtained self-consistently from the model. From an experimental standpoint, the analysis is restricted to gain values approaching 100 dB, corresponding to peak powers up to $P_p \approx 1.37$ kW. This parameter range is consistent with recent demonstrations of large parametric gain in dispersion-engineered thin-film lithium niobate WGs reaching 70–88 dB [72]. Table I describes the parameters used in the simulations.

A further point we investigate is how different poling profiles affect the gain-dependent evolution of the spectrum. Poling allows one to tailor the nonlinear response of a WG, and different patterns lead to distinct phase-matching functions [73]. In our study we consider two cases: unapodized WGs, which yield a sinc-type phase-matching function [74], and apodized WGs, engineered to produce a smoother, Gaussian-like phase-matching profile [75]. A detailed discussion of these phase-matching types is provided in Appendix B. The influence of these two phase-matching profiles on the spectral correlations of the generated two-mode squeezed states is examined in the following subsections.

To obtain the numerical results, we solve the coupled-mode equations [Eq. (17)] for the signal and idler modes for each phase-matching type. This yields the evolution of the complex functions introduced in Sec. II, which fully encode the field properties of the system. From these functions, we construct the second-order moment of the output state as defined in Eq. (19). For the Schmidt-mode analysis, we perform a singular value decomposition of this second-order moment, which provides the set of squeezing parameters. From these squeezing parameters, we compute the purity [Eq. (22)], the mode contributions [Eq. (25)], and the gain [Eq. (24)] used throughout this work.

A. Unapodized case

Figure 3 shows the simulated second moment of the squeezed state for an unapodized WG under three dispersion conditions $\theta = 0^\circ$, 45°, and -11° for a broadband pump. The top and bottom rows correspond to the low-gain (peak powers $P_p = 68.54$ and $27.78\ \mu$W) and high-gain (peak powers $P_p = 1.37$ and 0.56 kW) regimes, respectively. At low gain, the sinc-shaped phase-matching function produces visible sidelobes in all three cases. Across the three dispersion conditions, the spectral correlations are qualitatively different: nearly uncorrelated at $\theta = 0^\circ$, strongly correlated at $\theta = 45^\circ$, and anticorrelated at $\theta = -11^\circ$. At high gain, the second moment broadens and the low-gain sidelobes are suppressed in every case, a well-established effect in the high-gain regime [52].

Figure 4 illustrates the relationship between parametric gain and spectral purity for the considered dispersion conditions and pump bandwidths. Figure 4(a) corresponds to the broadband pump and shows that, at low gain, the dispersion conditions $\theta = 0^\circ$, 45°, and -11° have purities $\mathcal{P}$ of 0.913 (at $G_{\text{dB}} = 0.038$ dB), 0.409 (at $G_{\text{dB}} = 0.022$ dB), and 0.459 (at $G_{\text{dB}} = 0.042$ dB), respectively. As the gain increases, the purity rises in all the cases. However, the three dispersion conditions exhibit distinct gain-dependent dynamics: For $\theta = 0^\circ$ the state is nearly uncorrelated at low gain and its purity increases only gradually, for $\theta = 45^\circ$ the initially highly correlated state shows a rapid increase in purity with gain, and for $\theta = -11^\circ$ the purity increases at an intermediate rate. At high gain, the purities reach 0.991 (at $G_{\text{dB}} = 65.57$ dB), 0.999 (at $G_{\text{dB}} = 85.52$ dB), and 0.661 (at $G_{\text{dB}} = 98.95$ dB) for $\theta = 0^\circ$, 45°, and -11°, respectively.

Notably, although the $\theta = 0^\circ$ case starts with substantially higher spectral purity at low gain, the $\theta = 45^\circ$ curve overtakes it at intermediate gain [inset of Fig. 4(a)], with the crossing occurring near $G_{\text{dB}} \approx 26$ dB: $\theta = 45^\circ$ attains $\mathcal{P} = 0.965$ at $G_{\text{dB}} = 26.04$ dB, while $\theta = 0^\circ$ yields $\mathcal{P} = 0.962$ at $G_{\text{dB}} = 25.70$ dB. The initially correlated case also approaches $\mathcal{P} \approx 1$ at much lower gain than the $\theta = 0^\circ$ case. This demonstrates that a state with strong low-gain correlations can achieve higher purity at high gain than a nearly factorable state. Finally, the $\theta = -11^\circ$ case, where the purity remains well below unity over the tested gain range, demonstrates that there exist dispersion configurations which maintain a fundamentally multimode character, even at extreme values of gain.

In Fig. 4(b) the narrowband pump case is presented for the same dispersion conditions ($\theta = 0^\circ$, 45°, and -11°). Despite the low-gain purities differing significantly between the broadband and narrowband pump cases, the different dispersion configurations exhibit a qualitatively similar trend in

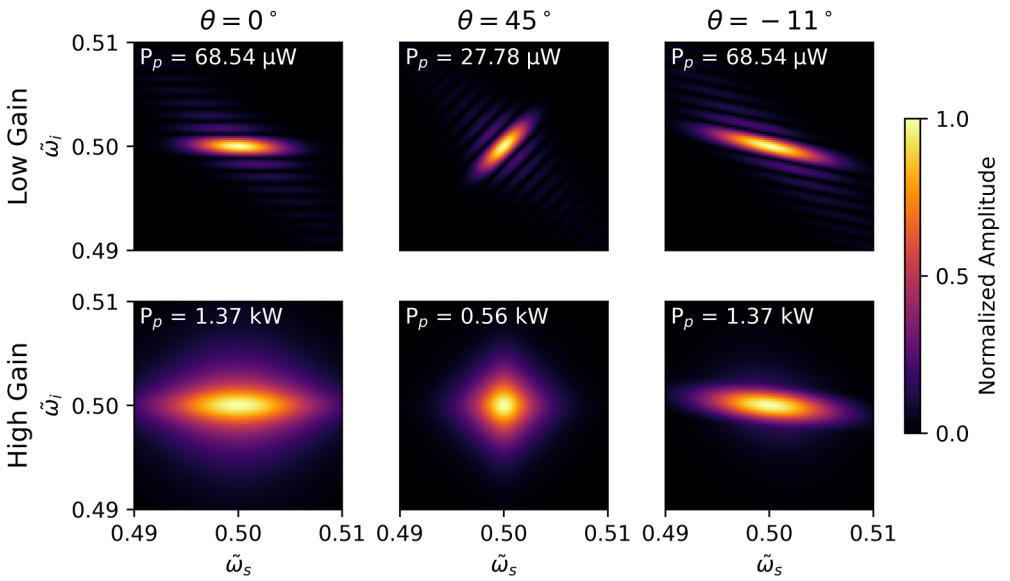


FIG. 3. Absolute value of the second moment of the two-mode squeezed state [Eq. (20)], which characterizes correlations between the signal and idler modes, for three dispersion conditions defined by the angles $\theta = 0^\circ$, 45°, and -11°. For each condition, two gain regimes are shown: low gain (peak powers $P_p = 68.54$ and 27.78 μW) and high gain (peak powers $P_p = 1.37$ and 0.56 kW). The frequency variables $\tilde{\omega}_s$ and $\tilde{\omega}_i$ are dimensionless, defined with respect to the central pump frequency ω_{p_0}. All panels are normalized to their respective maxima.

purity as a function of gain. This suggests that the observed gain-dependent dynamics is largely independent of pump bandwidth.

To gain more insight into the behavior seen in Fig. 4, we investigate the Schmidt-mode structure of the output spectrum. In particular, we consider the normalized contribution p_ℓ of each Schmidt mode to the total spectrum. In this analysis, we focus only on the broadband pump case for conciseness. Figure 5 shows the evolution of the normalized contributions of the three lowest-order Schmidt modes $p_{1,2,3}$ as a function of gain for $\theta = 0^\circ$, 45°, and -11°. In all cases, we see that the increase in spectral purity observed in Fig. 4 corresponds to a redistribution among the modes, with the lowest-order mode becoming more dominant at increasing gain, while the higher-order contributions decrease. This redistribution is relatively gradual for $\theta = 0^\circ$ and $\theta = -11^\circ$ [Figs. 5(a) and 5(b)] and in these cases is a well-known occurrence in high-gain PDC. More specifically, frequency components that are already favored by the phase-matching function and the pump envelope, i.e., near the central frequencies ω_{s0} and ω_{i0}, are more populated at lower gain and thus seed further down-conversion events at those frequencies more efficiently. As a result, the lowest-order Schmidt mode (which is centered around those frequencies) is preferentially amplified and its relative weight

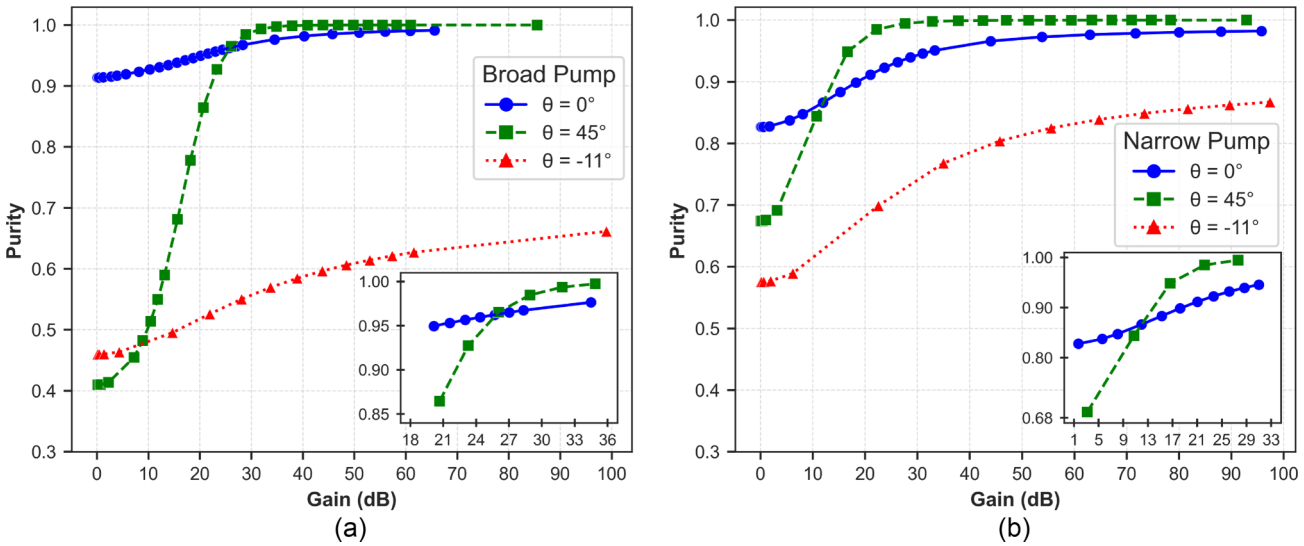


FIG. 4. Relationship between spectral purity and gain for three dispersion conditions defined by angles $\theta = 0^\circ$, 45°, and -11°, under both (a) broadband and (b) narrowband pump conditions. The inset highlights the crossing point of the spectral purity curves for the $\theta = 45^\circ$ and $\theta = 0^\circ$ conditions.

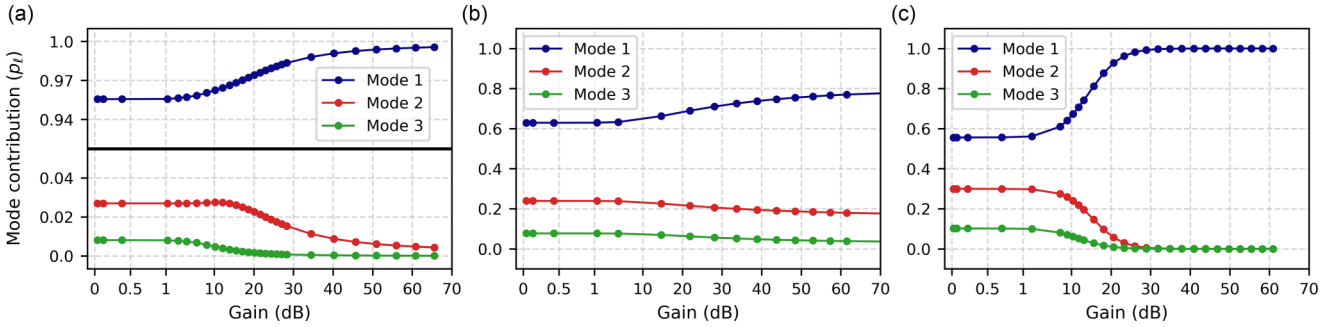


FIG. 5. Mode contribution p_ℓ of the first three Schmidt modes plotted versus gain for (a) $\theta = 0^\circ$, (b) $\theta = -11^\circ$, and (c) $\theta = 45^\circ$, for a broadband pump in an unapodized WG (sinc-type phase matching).

increases naturally with gain, while contributions from higher-order modes become less prominent [25,53,54,63].

For $\theta = 45^\circ$ [Fig. 5(c)], the higher-order mode contributions undergo a much sharper decline as gain increases, while the dominant mode p_1 rises steeply toward unity. As this redistribution of mode contributions is much faster than the other dispersion configurations, it is reasonable to assume that selective amplification of the lowest-order Schmidt mode mentioned above is here also accompanied by an additional mechanism that further suppresses higher-order Schmidt modes. To verify this, in Fig. 6 we plot the corresponding squeezing parameters $r^{(\ell)}$ of the three lowest-order Schmidt modes as a function of gain for the $\theta = 45^\circ$ configuration, as well as $\theta = 0^\circ$ for comparison. We first consider $\theta = 0^\circ$ as a baseline, shown in Fig. 6(a). We see that the squeezing factors for all of the Schmidt modes increase monotonically with gain, as predicted by previous works [25,54]. In contrast, Fig. 6(b) shows that the squeezing factors for the higher-order Schmidt modes in the $\theta = 45^\circ$ case reach a maximum value and then *decreases* with further gain. As this effect occurs within the same gain range as the rapid transfer of mode contributions in Fig. 5(c), we conclude that this reverse behavior of higher-order squeezing factors is the additional cause of the rapid purification of the spectrum in the $\theta = 45^\circ$ dispersion configuration.

To our knowledge, this kind of behavior has not been reported before in works on the spectral properties of high-gain, single-pass PDC in WGs. The fact that this effect only occurs in the dispersion configuration $\theta = 45^\circ$ and appears independent of the pump bandwidth suggests that the particular group-velocity configuration between the pump, signal, and idler fields is its main cause. However, before attempting to provide a physical interpretation of this effect, we will investigate whether it persists when the WG is apodized.

B. Apodized case

We now simulate the output spectrum of the apodized WG, where the phase-matching function is now Gaussian shaped. Figure 7 shows the second moment of this state under two dispersion conditions $\theta = 0^\circ$ and 45°, for a broadband pump. Here we omit the $\theta = -11^\circ$ configuration and focus on conditions that approach single-mode behavior at high gain. The top and bottom rows correspond to the low-gain ($P_p = 68.54$ and 27.78 μW) and high-gain ($P_p = 1.37$ and 0.56 kW) regimes, respectively. At low gain, the Gaussian phase-matching profile suppresses the side lobes observed in the unapodized case, as evident in Fig. 7 (top row). At high gain, the second moment broadens again, consistent with the behavior observed in the unapodized scenario.

We again quantitatively examine the spectral correlations of the two-mode squeezed state as a function of gain by analyzing its spectral purity. Figure 8 shows the

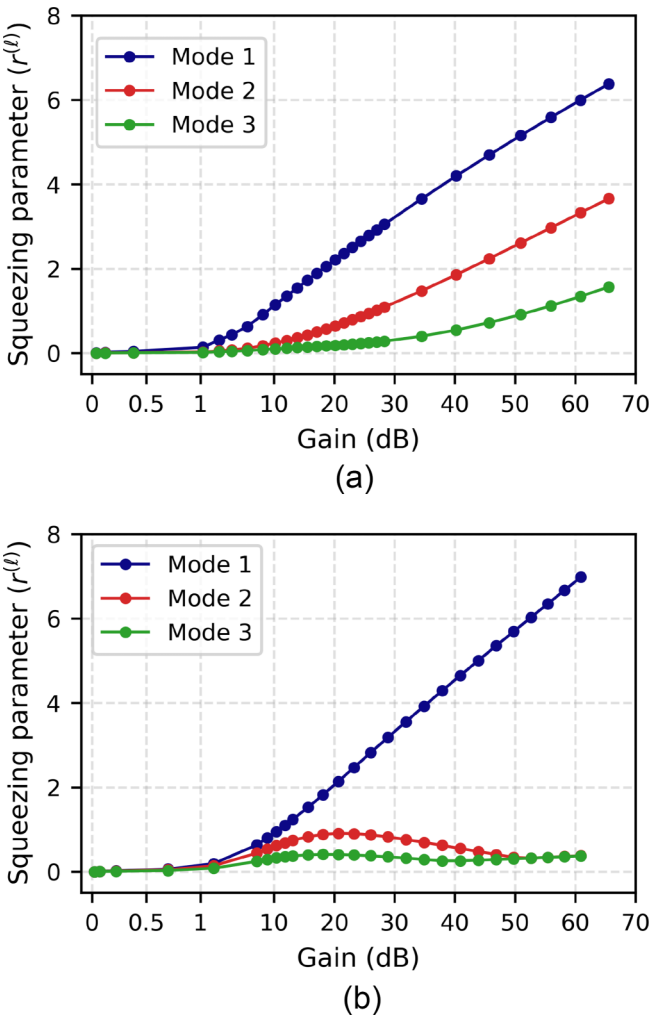


FIG. 6. Evolution of the first three squeezing parameters $r^{(\ell)}$ as a function of gain for (a) $\theta = 0^\circ$ and (b) $\theta = 45^\circ$, shown for the unapodized WG under broadband pumping.

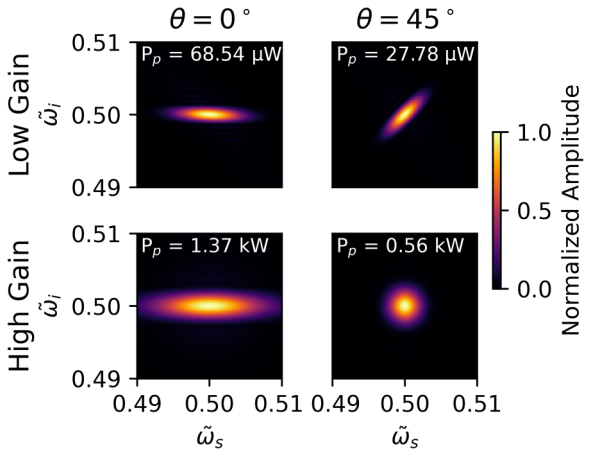


FIG. 7. Absolute value of the second moment of the squeezed state [Eq. (20)] for Gaussian-type phase matching under two dispersion settings $\theta = 0^\circ$ and 45°. For each setting, results are shown at two gain levels: low gain with peak pump powers $P_p = 68.54$ μW (for $\theta = 0^\circ$) and $P_p = 27.78$ μW (for $\theta = 45^\circ$) and high gain with $P_p = 1.37$ kW (for $\theta = 0^\circ$) and $P_p = 0.56$ kW (for $\theta = 45^\circ$). The frequency variables $\tilde{\omega}_s$ and $\tilde{\omega}_i$ are dimensionless, defined with respect to the central pump frequency ω_{p_0}. All panels are normalized to their respective maxima.

gain dependence of spectral purity for Gaussian-type phase matching under both broadband and narrowband pump conditions. In the broadband pump case, the low-gain purities $\mathcal{P}$ are 0.975 (at $G_{\mathrm{dB}} = 0.034$ dB) for $\theta = 0^\circ$ and 0.524 (at $G_{\mathrm{dB}} = 0.019$ dB) for $\theta = 45^\circ$. At high gain, although both dispersion conditions eventually reach very high purity, the $\theta = 45^\circ$ configuration achieves $\mathcal{P} = 0.999$ already at $G_{\mathrm{dB}} = 34.85$ dB, whereas the $\theta = 0^\circ$ case requires a substantially higher gain ($G_{\mathrm{dB}} = 92.38$ dB) to reach $\mathcal{P} = 0.995$.

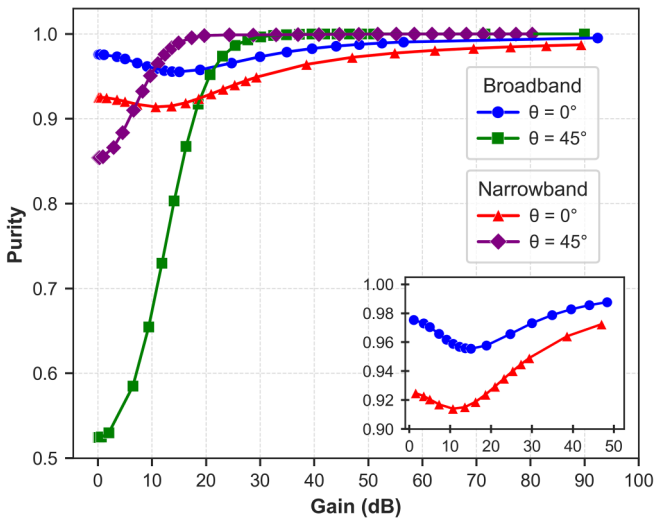


FIG. 8. Relationship between gain and spectral purity for Gaussian phase matching under two dispersion conditions $\theta = 0^\circ$ and $\theta = 45^\circ$ for both broadband and narrowband pump scenarios. The inset shows the nonmonotonic purity behavior for the $\theta = 0^\circ$ condition.

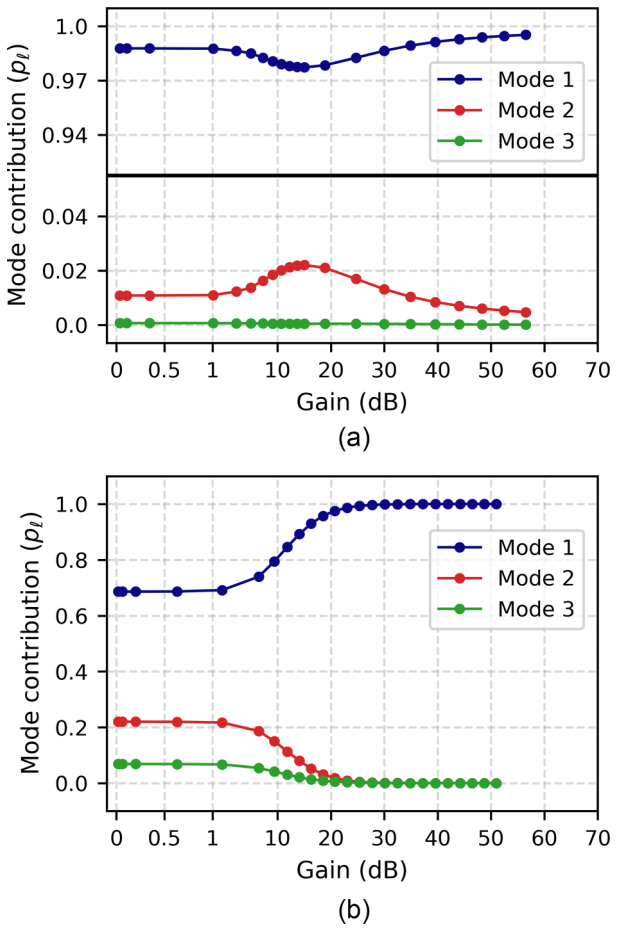


FIG. 9. Mode contribution p_ℓ of the first three Schmidt modes, plotted versus gain for a broadband pump in an apodized (Gaussian-type phase-matching) WG for (a) $\theta = 0^\circ$ and (b) $\theta = 45^\circ$.

For the narrowband pump case, we observe qualitatively similar purity behavior. Thus, the overall trend is consistent with the unapodized case: Purity improves at high gain, but we again see that $\theta = 45^\circ$ reaches higher purity values more rapidly than $\theta = 0^\circ$. This similarity suggests that this particular trend is also independent of the exact form of the phase-matching function, in addition to the pump bandwidth.

However, unlike the unapodized case, the apodized $\theta = 0^\circ$ case shows a distinct nonmonotonic behavior. Although it is nearly pure at low gain it exhibits a clear dip at moderate gain before again recovering at higher gain (see Fig. 8, inset). The monotonic decrease of the purity has been discussed in Refs. [59,76,77], where it was found to be due to additional phase correlations introduced in the joint spectrum as a consequence of seeding effects. Our results extend this picture by showing that, as gain is further increased, the purity rises again.

To analyze the above behaviors in more detail, we again investigate the gain-dependent Schmidt-mode structure of the output spectra and also only focus on the broadband pump for conciseness. In Fig. 9 the contributions of the first three Schmidt modes p_k are shown for the apodized configuration under two dispersion conditions $\theta = 0^\circ$ and 45°. At $\theta = 0^\circ$, the dominant mode contribution p_1 exhibits a shallow dip

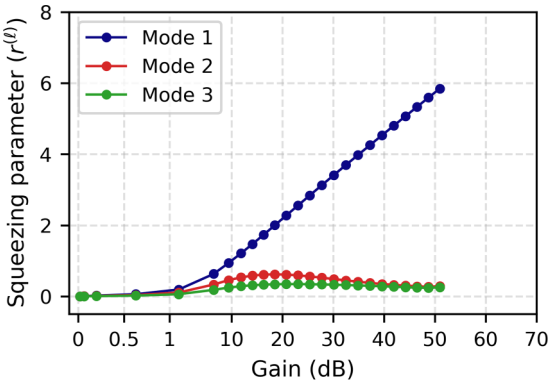


FIG. 10. Evolution of the first three squeezing parameters $r^{(\ell)}$ as a function of gain for the $\theta = 45^\circ$ case in the apodized WG.

at intermediate gain ($G_{\mathrm{dB}} \approx 15$ dB) before recovering toward unity. This mirrors the nonmonotonic trend observed in Fig. 8 and the temporary reduction in purity indeed corresponds to a redistribution of weight into higher-order modes. As gain is further increased, the lowest-order Schmidt mode is again more efficiently amplified, thereby suppressing these gain-induced correlations.

Now we turn our attention to the $\theta = 45^\circ$ case. We see that it follows the same trend as in the unapodized configuration: p_1 rapidly increases with gain, while higher-order contributions (p_2 and p_3) rapidly diminish. To further confirm that this is the same effect as observed in the unapodized WG, we again look at the gain dependence of the squeezing factors r_k for the $\theta = 45^\circ$ configuration. This is shown in Fig. 10 and we indeed see that the higher-order Schmidt modes are being additionally suppressed at high gain. The occurrence of this suppression effect for $\theta = 45^\circ$ also in the apodized WG reaffirms that it is primarily determined by the underlying group-velocity configuration. In the following, we present a physical explanation that accounts for this behavior across both phase-matching types.

C. Group-velocity-dependent purification mechanism

As already indicated, the observed additional suppression of higher-order Schmidt modes at high gain occurs in the $\theta = 45^\circ$ configuration, regardless of pump bandwidth and the type of phase matching. As the phase-matching angle θ is primarily dictated by the relative group velocities of the interacting modes [see Eq. (28)], it is reasonable to assume that such behavior is caused by high-gain seeding effects amplifying and modulating the effects of the temporal walk-off between the pump, signal, and idler [78–81].

When a pump pulse is sent to the nonlinear WG, over each small longitudinal slice of the WG, the three fields can interact and the contribution of each slice to the output joint spectrum includes a walk-off-induced phase [76–80]. At low gain, all slices contribute with approximately equal weight, and the interference of these uniformly weighted contributions produces the familiar low-gain phase-matching structure [78–80,82].

At high gain, however, the situation changes as seeding effects take hold [58,59,63,67,77]. Photon pairs generated earlier in the WG propagate for a longer distance before participating in further down-conversion and therefore accumulate more walk-off phase. Furthermore, each subsequent stimulated event inherits the phase of the field that seeded it, so the phase accumulated early in the WG is carried forward and amplified. On the other hand, photons generated later accumulate less phase but are more numerous, as high-gain PDC strongly favors pair creation near the WG output [76,82]. As a result, the effective weighting of the longitudinal slices becomes highly nonuniform, and the output joint spectrum, along with the spectral structure of the individual Schmidt modes, changes with gain [25,54,76,82].

In the $\theta = 45^\circ$ configuration, the group velocities satisfy $v_g^{(s)} < v_g^{(p)} < v_g^{(i)}$ and the signal and idler acquire walk-off phases of opposite sign. Thus the stimulated fields they generate downstream contribute to the output with likewise opposing signs and, as gain is increased, more and more such contributions appear. This introduces a new, gain-dependent interference mechanism which is most prominent for spectral components that already possess a nonzero phase at the output at low gain. Thus, it may lead such frequencies to potentially interfere destructively as gain is increased. Since higher-order Schmidt modes possess varying spectral phases, it is exactly their spectral components that are preferentially suppressed by this interference. In contrast, the lowest-order Schmidt mode has an almost flat spectral phase [59,63], so its amplification remains unaffected by the walk-off-induced interference.

Crucially, this mechanism does not rely on the perfect symmetry of the $\theta = 45^\circ$ case, which requires $v_g^{(p)}$ to lie halfway between $v_g^{(s)}$ and $v_g^{(i)}$, but to the overall group-velocity ordering $v_g^{(s)} < v_g^{(p)} < v_g^{(i)}$. This is sufficient to ensure that seeding effects generate frequency components with opposite phases with respect to the pump, leading in turn to destructive interference of higher-order Schmidt modes. To further verify this claim, we conducted additional simulations for $\theta = 40^\circ$, 42°, 47°, and 50°, which confirm that the same high-gain suppression of higher-order Schmidt modes occurs whenever the pump velocity lies between those of signal and idler. The results of those simulations are included in Appendix C, but they confirm that exact symmetry in the group-velocity configuration is not required.

In contrast, for the $\theta = 0^\circ$ configuration, $v_g^{(s)} = v_g^{(p)} < v_g^{(i)}$ and the walk-off phase contributions only come from the idler photons. In the $\theta = -11^\circ$ configuration, $v_g^{(p)} < v_g^{(s)} < v_g^{(i)}$ and the contributions from both photons have the same sign. Under such conditions, the effects of the gain-induced interference are much less prominent and there is no additional suppression of higher-order Schmidt modes, in accordance with our simulation results. These observations further confirm that the distinctive behavior seen in the $\theta = 45^\circ$ case originates from the pump lying between the signal and idler velocities, which alone enables the opposite-sign walk-off phases required for high-gain, interference-driven purification.

IV. CONCLUSION

We have studied the spectral properties of both unapodized and apodized dispersion-engineered WGs for the generation

of two-mode squeezed states in the high-gain regime. Our results show that the overall behavior of spectral purity as a function of gain, in both configurations, is primarily dictated by the dispersion conditions of the WG.

In the unapodized configuration, we considered three dispersion conditions $\theta = 0^\circ$, 45°, and -11°, each exhibiting a distinct gain-dependent evolution of spectral purity. For $\theta = 45^\circ$, the purity rises sharply with gain, whereas for $\theta = 0^\circ$ the increase is more gradual, though it still approaches near unity at high gain. In contrast, the $\theta = -11^\circ$ case remains fundamentally multimode, with purity remaining well below unity. In the apodized configuration, the $\theta = 45^\circ$ case again shows a monotonic increase in purity, while the $\theta = 0^\circ$ configuration exhibits nonmonotonic behavior: The purity initially decreases due to gain-induced phase correlations and later recovers at higher gain. Previous studies such as Ref. [76] reported only a monotonic decrease. Our results extend this understanding of gain-dependent dynamics by showing that purity can recover once the lowest-order Schmidt mode becomes strongly dominant.

A key outcome of our study is the identification of a distinct high-gain suppression mechanism for higher-order Schmidt modes. In the dispersion configuration where the pump group velocity lies between those of the signal and idler ($v_g^{(s)} < v_g^{(p)} < v_g^{(i)}$, corresponding to $\theta = 45^\circ$), the squeezing parameters of higher-order Schmidt modes do not merely saturate but begin to decrease at sufficiently high gain. This leads to a markedly faster purification of the output state compared to other dispersion settings. By combining Schmidt-mode analysis with a group-velocity-based interpretation, we attribute this behavior to a gain-induced interference mechanism driven by the opposite-sign walk-off phases of the signal and idler fields. Additional simulations for nearby dispersion angles ($\theta = 40^\circ, 42^\circ, 47^\circ, 50^\circ$) show that this effect is robust and does not rely on fine-tuning or perfect symmetry; it appears whenever the pump group velocity lies between those of the signal and idler. Moreover, the gain-dependent behavior, including the rapid purification in the $\theta = 45^\circ$ configuration, is insensitive to the pump bandwidth and to the detailed form of the phase-matching function (sinc or Gaussian). This demonstrates that the mechanism is fundamentally dictated by the dispersion relations of the interacting modes, rather than by the pump bandwidth or phase-matching function.

From an experimental standpoint, the $\theta = 45^\circ$ configuration is especially attractive because it allows the degree of spectral entanglement to be tuned solely through the parametric gain. As a result, the same WG can function either as a strongly entangled, multimode source or as an almost single-mode source, depending on the desired regime. This gain-based tunability provides a flexible and compact tool for integrated quantum photonics.

In summary, our work highlights the central role of dispersion engineering in shaping high-gain PDC spectra and uncovers a previously unreported mechanism through which specific group-velocity configurations induce accelerated purification at high gain. These insights provide practical design principles for developing squeezed-light sources tailored to the requirements of diverse quantum technologies.

ACKNOWLEDGMENTS

This research was funded by the German Federal Ministry of Research, Technology and Space (BMFTR) Projects No. 13N16108 PhoQuant and No. 13N16975 LichtBriQ. This research was supported by funding from the Carl-Zeiss-Stiftung Center QPhoton. S.S. acknowledges funding from the Nexus program of the Carl-Zeiss-Stiftung (MetaNN, Project No. P2022-04-018).

DATA AVAILABILITY

The PYTHON code used for the simulations and figure generation, and the simulated data supporting the findings of this study are openly available from [83].

APPENDIX A: LOW-GAIN SOLUTION OF THE JOINT SPECTRAL AMPLITUDE

In the low-gain regime, we solve the coupled integral (17) from the main text perturbatively. We begin by initializing the complex function $A(\omega_s, \omega_s'', t)$ at the initial time t_0 and then solve the following time-dependent differential equation to determine the evolution of the complex function $D(\omega_i', \omega_s'', t)$:

$$\partial_t D(\omega_i', \omega_s'', t) = -\frac{i}{\hbar}\int_0^\infty \mathrm{d}\omega_s G_2(\omega_s, \omega_i', t) A^*(\omega_s, \omega_s'', t). \tag{A1}$$

We impose the initial condition

$$A(\omega_s, \omega_s'', t_0) = \delta(\omega_s - \omega_s'') \tag{A2}$$

and substitute this into the evolution equation to obtain

$$\begin{aligned}\partial_t D(\omega_i', \omega_s'', t) &= -\frac{i}{\hbar}\int_0^\infty \mathrm{d}\omega_s G_2(\omega_s, \omega_i', t)\delta(\omega_s - \omega_s'') \\ &= -\frac{i}{\hbar} G_2(\omega_s'', \omega_i', t).\end{aligned} \tag{A3}$$

Integrating both sides with respect to time yields the solution

$$D(\omega_i', \omega_s'', t) = -\frac{i}{\hbar}\int \mathrm{d}t\, G_2(\omega_s'', \omega_i', t). \tag{A4}$$

We now express $G_2(\omega_s'', \omega_i', t)$ using system parameters and obtain

$$\begin{aligned}D(\omega_i', \omega_s'', t) = -i\frac{M\gamma_p}{2\pi c}&\sqrt{\omega_i'\omega_s'' n_g^i(\omega_i') n_g^s(\omega_s'') n_g^p(\omega_{p_0})} \\ &\times \int_0^\infty \mathrm{d}\omega_p \alpha(\omega_p)\phi\left(\frac{\Delta k(\omega_s'', \omega_i', \omega_p)L}{2}\right) \\ &\times \int_{t_0}^t \mathrm{d}t\, \exp[-i(\omega_p - \omega_s'' - \omega_i')t].\end{aligned} \tag{A5}$$

We evaluate the time integral assuming that there is a long interaction time which is given as

$$\int_{-\infty}^\infty \mathrm{d}t\, \exp[-i(\omega_p - \omega_s'' - \omega_i')t] = 2\pi\delta(\omega_p - \omega_s'' - \omega_i'), \tag{A6}$$

which yields the simplified expression

$$D(\omega_i', \omega_s'') = -i\frac{M\gamma_p}{c}\sqrt{\omega_i'\omega_s'' n_g^i(\omega_i') n_g^s(\omega_s'') n_g^p(\omega_{p_0})} \times \alpha(\omega_i' + \omega_s'')\phi\left(\frac{\Delta k(\omega_s'', \omega_i', \omega_i' + \omega_s'')L}{2}\right). \tag{A7}$$

Next we compute the second-order moment using Eq. (19):

$$\begin{aligned}\langle 0|\tilde{a}_{\omega_s}(t)\tilde{b}_{\omega_i}(t)|0\rangle &= \int \mathrm{d}\omega_s'' A(\omega_s, \omega_s'', t) D(\omega_i, \omega_s'', t) \\ &= \int \mathrm{d}\omega_s'' \delta(\omega_s - \omega_s'') D(\omega_i, \omega_s'') \\ &= D(\omega_i, \omega_s).\end{aligned} \tag{A8}$$

Thus, the JSA in the low-gain regime is given by

$$\begin{aligned}J(\omega_s, \omega_i) &= D(\omega_i, \omega_s) \\ &= \zeta\alpha(\omega_s + \omega_i)\phi\left(\frac{\Delta k(\omega_s, \omega_i)L}{2}\right),\end{aligned} \tag{A9}$$

where the prefactor ζ is calculated assuming that the overlap integral and group indices have small variations with respect to the frequency which is given as

$$\zeta = -i\frac{\gamma_p M}{c}\sqrt{\omega_i\omega_s n_g^i(\omega_i) n_g^s(\omega_s) n_g^p(\omega_{p_0})}. \tag{A10}$$

This expression captures the spectral correlations at low gain.

APPENDIX B: GENERALIZED PHASE MATCHING

The generalized phase-matching function in Eq. (9) depends on the longitudinal modulation of the nonlinear coefficient, which we model as

$$\chi^{(2)}(z) = df(z), \quad f(z) \in \{+1, -1\}.$$

In periodically poled WGs, $f(z)$ alternates between $+1$ and -1 with a fixed poling period Λ and duty cycle $D \in (0, 1)$. This periodic reversal of the nonlinear coefficient implements quasi-phase-matching (QPM) by compensating for the accumulated phase mismatch between the interacting waves.

To understand how the choice of poling pattern determines the phase-matching function, it is useful to expand the modulation function $f(z)$ into a Fourier series [73]

$$f(z) = \sum_{m\in\mathbb{Z}} f_m e^{imKz}, \quad K = \frac{2\pi}{\Lambda},$$

with Fourier coefficients

$$\begin{aligned}f_m &= \frac{1}{\Lambda}\int_0^\Lambda f(z)e^{-imKz}dz \\ &= \begin{cases}2D - 1, & m = 0 \\ \frac{2}{m\pi}e^{-im\pi D}\sin(m\pi D), & m \neq 0.\end{cases}\end{aligned}$$

In practice, periodically poled WGs are fabricated with a 50% duty cycle ($D = \frac{1}{2}$) [84,85]. In this case, the dc component of the nonlinear grating vanishes ($f_0 = 0$), meaning that the average nonlinear coefficient over one period is zero, and only odd Fourier harmonics remain. The first-order coefficients are

$$f_{\pm1} = \mp\frac{2i}{\pi}, \quad |f_1| = \frac{2}{\pi}.$$

Higher-order harmonics ($|m| \geqslant 3$) oscillate much more rapidly along the WG and therefore contribute only weakly to the phase-matching integral, as they largely average out over the device length. For this reason, experimental analyses typically retain only the dominant first-order QPM term. Under this approximation, the spatial modulation of the nonlinear coefficient reduces to

$$f(z) \approx f_1 e^{iKz} + f_{-1}e^{-iKz} = \frac{4}{\pi}\sin(Kz)$$

and the effective nonlinear coefficient becomes

$$d_{\mathrm{eff}} = \frac{2}{\pi}d.$$

When this modulation is integrated over the crystal length, the resulting phase-matching function is

$$\phi\left(\frac{\Delta kL}{2}\right) = \frac{2}{\pi}\mathrm{sinc}\left(\frac{(\Delta k - 2\pi/\Lambda)L}{2}\right) \times \exp\left(i\frac{(\Delta k - 2\pi/\Lambda)L}{2}\right).$$

This sinc-type phase-matching response (the unapodized case used in the main text) arises from the first-order quasi-phase-matched interaction integrated over a finite crystal length L. Its characteristic side lobes introduce spectral oscillations in the joint spectrum and are one of the dominant sources of spectral correlations in low-gain PDC.

In contrast, an apodized (aperiodically poled) WG intentionally modulates the poling pattern slowly along the propagation direction. By allowing the poling period $\Lambda(z)$ or the duty cycle $D(z)$ to vary gradually with z, the amplitude and phase of the first Fourier harmonic acquire a smooth spatial envelope [75,86]:

$$|f_1(z)| = \frac{2}{\pi}|\sin[\pi D(z)]|, \quad \arg f_1(z) = -\pi D(z).$$

Through this slow modulation, the effective spatial dependence of the nonlinear interaction is smoothly shaped along the propagation direction. Since the side lobes of the sinc-type phase-matching response arise from a uniform interaction over a finite length, this shaping suppresses those side lobes and yields a smooth, approximately Gaussian phase-matching envelope.

Apodization may thus be viewed as convolving the uniform-grating response with a slowly varying envelope function. In the limit where the envelope is chosen to be Gaussian, the resulting phase-matching function is well approximated by

$$\phi_{\mathrm{apo}}\left(\frac{\Delta kL}{2}\right) \propto \exp\left(-\frac{(\Delta kL)^2\sigma^2}{2}\right),$$

where σ characterizes the effective width of the nonlinear interaction region. This Gaussian-like phase-matching function suppresses side lobes and yields smoother JSAs at low gain, which is the apodized configuration used in the main text.

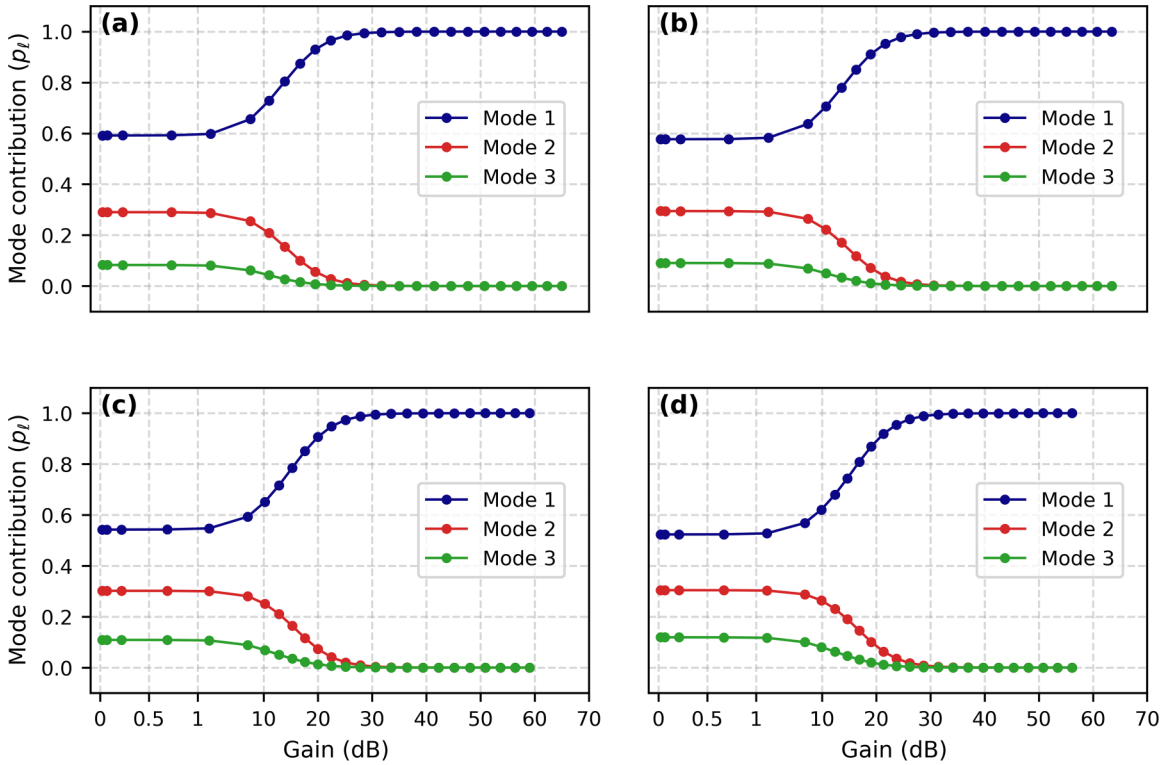


FIG. 11. Mode contribution p_ℓ of the first three Schmidt modes plotted versus gain for (a) $\theta = 40^\circ$, (b) $\theta = 42^\circ$, (c) $\theta = 47^\circ$, and (d) $\theta = 50^\circ$, for a broadband pump in an unapodized WG (sinc-type phase matching).

In summary, the unapodized case naturally yields the standard sinc-type phase-matching function, while controlled apodization enables the nonlinear profile to be engineered such that the resulting phase-matching response becomes smooth and approximately Gaussian. These two limiting cases form the basis for the comparison performed in Sec. III.

APPENDIX C: OTHER GROUP-VELOCITY CONFIGURATIONS

As discussed in the main text, the dispersion configuration with $\theta = 45^\circ$ exhibits a characteristic high-gain suppression of higher-order Schmidt modes. In this appendix we show that the same behavior persists for nearby dispersion angles, specifically $\theta = 40^\circ$, 42°, 47°, and 50°, all of which satisfy the group-velocity ordering $v_g^{(s)} < v_g^{(p)} < v_g^{(i)}$.

Figure 11 shows the gain dependence of the mode contributions p_ℓ for the first three Schmidt modes under these four dispersion configurations. In all cases, the contribution of the first Schmidt mode increases rapidly with gain, while the second and third mode contributions decrease correspondingly.

This behavior mirrors the dynamics observed for the $\theta = 45^\circ$ case and confirms that the effect is not tied to a finely tuned symmetric point. Instead, it consistently appears whenever the pump group velocity lies between those of the signal and idler. As explained in Sec. III C, this arises from the gain-dependent interference mechanism driven by the opposite-sign walk-off phases of the signal and idler fields. The results presented here therefore support the conclusion that the underlying mechanism is robust to small variations in the phase-matching angle and is dictated primarily by the qualitative ordering of group velocities rather than the precise value of θ.

APPENDIX D: LIMITATIONS OF THE CURRENT SIMULATIONS

In the simulations presented in this work, we neglect pump depletion and Kerr-induced phase modulation and retain only first-order dispersion. These approximations allow us to isolate the $\chi^{(2)}$-driven high-gain dynamics and the role of relative group-velocity ordering in the evolution of the spectral modes. In this appendix we estimate the validity of these approximations in the parameter regime considered here.

1. Pump depletion

The undepleted-pump approximation is valid only when the number of generated photon pairs remains much smaller than the number of pump photons in each pulse [87]. We quantify this condition using the depletion fraction

$$f_{\text{dep}} = \frac{N_{\text{pairs}}}{N_p}, \tag{D1}$$

where N_{pairs} is the total generated photon-pair number and N_p is the number of pump photons per pulse. When f_{dep} reaches the percent level, for example, $f_{\text{dep}} \sim 10^{-2}$, the conversion of pump photons into photon pairs is no longer negligible. The pump field can then no longer be treated as a fixed classical input. In that regime, a depleted-pump model is required because the pump, signal, and idler dynamics become fully coupled, and the present framework based on the

undepleted-pump approximation is no longer sufficient. For the Gaussian pump envelope used in our simulations, the pulse energy is

$$E_p = P_p\sqrt{\pi}\sigma_t, \tag{D2}$$

where P_p and σ_t are the peak pump power and temporal pump-envelope width defined in the main text, respectively. The corresponding number of pump photons per pulse is

$$N_p = \frac{E_p}{\hbar\omega_{p_0}}. \tag{D3}$$

We evaluate this estimate at the highest-gain point considered in the simulations, $P_p = 1370.78$ W and $G = 98.96$ dB, for which the total generated photon-pair number is $N_{\text{pairs}} \approx 9.98 \times 10^4$. Using $\sigma_t = 137.05$ fs and $\omega_{p_0} = 2.43 \times 10^{15}$ s^{-1}, we obtain $N_p \approx 1.30 \times 10^9$. The resulting depletion fraction is $f_{\text{dep}} \approx 7.68 \times 10^{-5}$, corresponding to only 0.0077% pump depletion. Thus, pump depletion is negligible in the parameter regime considered here.

2. Kerr-induced phase modulation

The simulations presented in this work isolate the $\chi^{(2)}$-driven high-gain dynamics and do not include $\chi^{(3)}$-induced Kerr effects such as self-phase modulation (SPM) and cross-phase modulation (XPM). This allows us to focus on the role of $\chi^{(2)}$ dispersion engineering alone. These effects can nevertheless be incorporated within the Bogoliubov-transformation formalism by adding the corresponding SPM and XPM Hamiltonian terms. Under the undepleted-pump approximation, the pump-SPM Hamiltonian modifies the classical pump field through an intensity-dependent nonlinear phase. Pump-induced XPM, on the other hand, enters as number-conserving quadratic terms of the form $\hat{a}_j^\dagger(\omega)\hat{a}_j(\omega')$, with $j = s, i$, in the signal and idler operators [58]. Therefore, XPM does not generate signal-idler pairs by itself, but it can modify the propagation phases and modal structure.

To estimate when Kerr-induced phase modulation may become relevant, we consider the accumulated nonlinear phases [88]

$$\phi_{\text{SPM}}^{\max} \approx \Gamma_p P_p L, \quad \Gamma_p = \frac{2\pi n_2}{\lambda_p A_{\text{eff}}^{(p)}}, \tag{D4}$$

and

$$\phi_{\text{XPM},j}^{\max} \approx 2\Gamma_{jp} P_p L, \quad \Gamma_{jp} = \frac{2\pi n_2}{\lambda_j A_{\text{eff}}^{(jp)}}, \ j = s, i. \tag{D5}$$

Here n_2 is the Kerr nonlinear index, $A_{\text{eff}}^{(p)}$ is the effective pump mode area, and $A_{\text{eff}}^{(jp)}$ denotes the effective pump-signal or pump-idler overlap area. Taking representative order-of-magnitude values $n_2 \sim 2 \times 10^{-19}$ m^2/W [89] and $A_{\text{eff}} \sim 1$ μm^2, we obtain $\Gamma \sim 1.62$ W^{-1} m^{-1} using $\lambda_p = 775$ nm. For a 5-mm WG, this gives

$$\phi_{\text{SPM}}^{\max} \approx (0.008)P_p, \quad \phi_{\text{XPM}}^{\max} \approx (0.016)P_p, \tag{D6}$$

with P_p in watts. Thus, SPM reaches an order-unity phase at $P_p \approx 123$ W, while XPM reaches an order-unity phase at $P_p \approx 62$ W. For the 2.5-mm case, the corresponding threshold powers are doubled within this estimate.

Mapping these estimates onto the simulated gain values for the broadband-pump cases, for the $\theta = 0^\circ$ case with a 5-mm interaction length, the XPM thresholds correspond to $G \approx 13$ dB for sinc phase matching and $G \approx 11.5$ dB for Gaussian phase matching. The corresponding SPM thresholds are $G \approx 20$ and 17.6 dB, respectively. For the $\theta = 45^\circ$ case with a 2.5-mm interaction length, the XPM thresholds shift to $G \approx 17$ and 15 dB, while the SPM thresholds become $G \approx 28.5$ and 25 dB, for the sinc and Gaussian phase-matching cases, respectively.

These estimates suggest that Kerr-induced phase modulation can become relevant already at moderate gain values in the parameter ranges considered here. When SPM and XPM are included, the spectral phases and effective phase matching can be quantitatively modified, leading to changes in the spectral correlations and modal structure. The gain-dependent purity trends reported here should therefore be understood as the $\chi^{(2)}$-only limit.

3. Group-velocity dispersion

The theoretical formalism presented in this paper can in principle include arbitrary dispersion through the full frequency-dependent propagation constants. In the present simulations, however, we retain only the first-order dispersion terms, corresponding to the group velocities of the pump, signal, and idler fields. This allows us to isolate the role of relative group-velocity ordering in the gain-dependent evolution of the spectral modes.

To estimate the relevance of group-velocity dispersion (GVD) in the present parameter regime, we compare the device length L with the dispersion length [88]

$$L_D = \frac{\sigma_t^2}{|\beta_2|}, \tag{D7}$$

where σ_t is the temporal pump-envelope width and β_2 is the second-order dispersion parameter. Taking a representative value $|\beta_2| \approx 100$ fs^2/mm [90–92], we obtain $L_D \approx 188$ mm for $\sigma_t = 137.05$ fs and $L_D \approx 751$ mm for $\sigma_t = 274.10$ fs. For the longest WG considered here, $L = 5$ mm, this gives $L/L_D \approx 2.7 \times 10^{-2}$ and 6.7×10^{-3}, respectively.

Thus, the simulations lie in a weak-GVD regime ($L/L_D \ll 1$), where GVD-induced pulse reshaping is expected to be small for the pulse durations and WG lengths considered here. Nevertheless, GVD can affect the detailed spectral correlations and modal structure for shorter pulses, longer devices, or larger $|\beta_2|$, where L_D becomes comparable to L. In that regime, the simple group-velocity-ordering picture may no longer be sufficient. Related high-gain type-II PDC theory has shown that second-order dispersion can produce gain-induced spectral shifts and a transition from degenerate to nondegenerate emission, thereby modifying the distinguishability and spectral correlations of the generated photons [93].

[1] S. Slussarenko and G. J. Pryde, Photonic quantum information processing: A concise review, Appl. Phys. Rev. **6**, 041303 (2019).

[2] M. Gilaberte Basset, F. Setzpfandt, F. Steinlechner, E. Beckert, T. Pertsch, and M. Gräfe, Perspectives for applications of quantum imaging, Laser Photon. Rev. **13**, 1900097 (2019).

[3] E. Polino, M. Valeri, N. Spagnolo, and F. Sciarrino, Photonic quantum metrology, AVS Quantum Sci. **2**, 024703 (2020).

[4] B. J. Lawrie, P. D. Lett, A. M. Marino, and R. C. Pooser, Quantum sensing with squeezed light, ACS Photon. **6**, 1307 (2019).

[5] U. L. Andersen, G. Leuchs, and C. Silberhorn, Continuous-variable quantum information processing, Laser Photon. Rev. **4**, 337 (2010).

[6] S. L. Braunstein and P. van Loock, Quantum information with continuous variables, Rev. Mod. Phys. **77**, 513 (2005).

[7] C. S. Hamilton, R. Kruse, L. Sansoni, S. Barkhofen, C. Silberhorn, and I. Jex, Gaussian boson sampling, Phys. Rev. Lett. **119**, 170501 (2017).

[8] H.-S. Zhong, Y.-H. Deng, J. Qin, H. Wang, M.-C. Chen, L.-C. Peng, Y.-H. Luo, D. Wu, S.-Q. Gong, H. Su, Y. Hu, P. Hu, X.-Y. Yang, W.-J. Zhang, H. Li, Y. Li, X. Jiang, L. Gan, G. Yang, L. You, *et al.*, Phase-programmable Gaussian boson sampling using stimulated squeezed light, Phys. Rev. Lett. **127**, 180502 (2021).

[9] Z. Vernon, N. Quesada, M. Liscidini, B. Morrison, M. Menotti, K. Tan, and J. E. Sipe, Scalable squeezed-light source for continuous-variable quantum sampling, Phys. Rev. Appl. **12**, 064024 (2019).

[10] L. Madsen, V. Usenko, M. Lassen, R. Filip, and U. L. Andersen, Continuous variable quantum key distribution with modulated entangled states, Nat. Commun. **3**, 1083 (2012).

[11] Y.-C. Zhang, Z. Li, S. Yu, W. Gu, X. Peng, and H. Guo, Continuous-variable measurement-device-independent quantum key distribution using squeezed states, Phys. Rev. A **90**, 052325 (2014).

[12] I. Derkach, V. C. Usenko, and R. Filip, Squeezing-enhanced quantum key distribution over atmospheric channels, New J. Phys. **22**, 053006 (2020).

[13] M. I. Kolobov and P. Kumar, Sub-shot-noise microscopy: Imaging of faint phase objects with squeezed light, Opt. Lett. **18**, 849 (1993).

[14] G. Brida, M. Genovese, and I. R. Berchera, Experimental realization of sub-shot-noise quantum imaging, Nat. Photon. **4**, 227 (2010).

[15] M. A. Taylor, J. Janousek, V. Daria, J. Knittel, B. Hage, H.-A. Bachor, and W. P. Bowen, Subdiffraction-limited quantum imaging within a living cell, Phys. Rev. X **4**, 011017 (2014).

[16] C. M. Caves, Quantum-mechanical noise in an interferometer, Phys. Rev. D **23**, 1693 (1981).

[17] V. Giovannetti, S. Lloyd, and L. Maccone, Advances in quantum metrology, Nat. Photon. **5**, 222 (2011).

[18] J. Aasi, J. Abadie, B. P. Abbott, R. Abbott, T. D. Abbott, M. R. Abernathy, C. Adams, T. Adams, P. Addesso, *et al.*, Enhanced sensitivity of the LIGO gravitational wave detector by using squeezed states of light, Nat. Photon. **7**, 613 (2013).

[19] R. E. Slusher, L. W. Hollberg, B. Yurke, J. C. Mertz, and J. F. Valley, Observation of squeezed states generated by four-wave mixing in an optical cavity, Phys. Rev. Lett. **55**, 2409 (1985).

[20] L.-A. Wu, H. J. Kimble, J. L. Hall, and H. Wu, Generation of squeezed states by parametric down conversion, Phys. Rev. Lett. **57**, 2520 (1986).

[21] R. M. Shelby, M. D. Levenson, S. H. Perlmutter, R. G. DeVoe, and D. F. Walls, Broad-band parametric deamplification of quantum noise in an optical fiber, Phys. Rev. Lett. **57**, 691 (1986).

[22] R. Loudon and P. L. Knight, Squeezed light, J. Mod. Opt. **34**, 709 (1987).

[23] R. S. Bennink, Y. Liu, D. D. Earl, and W. P. Grice, Spatial distinguishability of photons produced by spontaneous parametric down-conversion with a focused pump, Phys. Rev. A **74**, 023802 (2006).

[24] E. Brambilla, A. Gatti, M. Bache, and L. A. Lugiato, Simultaneous near-field and far-field spatial quantum correlations in the high-gain regime of parametric down-conversion, Phys. Rev. A **69**, 023802 (2004).

[25] P. R. Sharapova, G. Frascella, M. Riabinin, A. M. Pérez, O. V. Tikhonova, S. Lemieux, R. W. Boyd, G. Leuchs, and M. V. Chekhova, Properties of bright squeezed vacuum at increasing brightness, Phys. Rev. Res. **2**, 013371 (2020).

[26] T. Iskhakov, M. V. Chekhova, and G. Leuchs, Generation and direct detection of broadband mesoscopic polarization-squeezed vacuum, Phys. Rev. Lett. **102**, 183602 (2009).

[27] U. L. Andersen, T. Gehring, C. Marquardt, and G. Leuchs, 30 years of squeezed light generation, Phys. Scr. **91**, 053001 (2016).

[28] A. I. Lvovsky and M. G. Raymer, Continuous-variable optical quantum-state tomography, Rev. Mod. Phys. **81**, 299 (2009).

[29] M. A. Taylor and W. P. Bowen, Quantum metrology and its application in biology, Phys. Rep. **615**, 1 (2016).

[30] F. Lenzini, J. Janousek, S. Zhang, O. Thearle, S. Knabe, Y.-W. Choi, T. Gerrits, O. Slattery, S. W. Nam, G. Walker, L. Neumeier, C. Husko, B. J. Eggleton, E. H. Huntington, T. C. Ralph, A. G. White, L.-C. Kwek, M. Lobino, and L. S. Madsen, Integrated photonic platform for quantum information with continuous variables, Sci. Adv. **4**, eaat9331 (2018).

[31] H. Kogelnik, An introduction to integrated optics, IEEE Trans. Microwave Theory Tech. **23**, 2 (1975).

[32] J. W. Silverstone, D. Bonneau, J. L. O'Brien, and M. G. Thompson, Silicon quantum photonics, IEEE J. Sel. Top. Quantum Electron. **22**, 390 (2016).

[33] S. Tanzilli, A. Martin, F. Kaiser, M. P. De Micheli, O. Alibart, and D. B. Ostrowsky, On the genesis and evolution of integrated quantum optics, Laser Photon. Rev. **6**, 115 (2012).

[34] D. B. Horoshko, M. I. Kolobov, V. Parigi, and N. Treps, Few-mode squeezing in type-I parametric downconversion by complete group velocity matching, Opt. Lett. **49**, 4078 (2024).

[35] C. Wang, M. Zhang, X. Chen, M. Bertrand, A. Shams-Ansari, S. Chandrasekhar, P. Winzer, and M. Lončar, Integrated lithium niobate electro-optic modulators operating at CMOS-compatible voltages, Nature (London) **562**, 101 (2018).

[36] J. Wang, S. Paesani, Y. Ding, R. Santagati, P. Skrzypczyk, A. Salavrakos, J. Tura, R. Augusiak, L. Mančinska, D. Bacco, D. Bonneau, J. W. Silverstone, M. G. Thompson, G. Vallone, A. Laing, A. Acín, K. Rottwitt, L. K. Oxenløwe, J. L. O'Brien, J. Wang, *et al.*, Multidimensional quantum entanglement with large-scale integrated optics, Science **360**, 285 (2018).

[37] K. Garay-Palmett, H. J. McGuinness, O. Cohen, J. S. Lundeen, R. Rangel-Rojo, A. B. U'Ren, M. G. Raymer, C. J. McKinstrie,

S. Radic, and I. A. Walmsley, Photon pair-state preparation with tailored spectral properties by spontaneous four-wave mixing in photonic-crystal fiber, Opt. Express **15**, 14870 (2007).

[38] O. Cohen, J. S. Lundeen, B. J. Smith, G. Puentes, P. J. Mosley, and I. A. Walmsley, Tailored photon-pair generation in optical fibers, Phys. Rev. Lett. **102**, 123603 (2009).

[39] C. Söller, B. Brecht, P. J. Mosley, L. Y. Zang, A. Podlipensky, N. Y. Joly, P. S. J. Russell, and C. Silberhorn, Bridging visible and telecom wavelengths with a single-mode broadband photon pair source, Phys. Rev. A **81**, 031801(R) (2010).

[40] X. Guo, N. Liu, X. Li, and Z. Y. Ou, Complete temporal mode analysis in pulse-pumped fiber-optical parametric amplifier for continuous variable entanglement generation, Opt. Express **23**, 29369 (2015).

[41] N. Liu, Y. Liu, X. Guo, L. Yang, X. Li, and Z. Ou, Approaching single temporal mode operation in twin beams generated by pulse pumped high gain spontaneous four wave mixing, Opt. Express **24**, 1096 (2016).

[42] M. A. Finger, N. Y. Joly, P. S. J. Russell, and M. V. Chekhova, Characterization and shaping of the time-frequency Schmidt mode spectrum of bright twin beams generated in gas-filled hollow-core photonic crystal fibers, Phys. Rev. A **95**, 053814 (2017).

[43] A. W. Bruch, X. Liu, J. B. Surya, C.-L. Zou, and H. X. Tang, On-chip $\chi^{(2)}$ microring optical parametric oscillator, Optica **6**, 1361 (2019).

[44] J. Lu, A. A. Sayem, Z. Gong, J. B. Surya, C.-L. Zou, and H. X. Tang, Ultralow-threshold thin-film lithium niobate optical parametric oscillator, Optica **8**, 539 (2021).

[45] T. Park, H. Stokowski, V. Ansari, S. Gyger, K. K. S. Multani, O. T. Celik, A. Y. Hwang, D. J. Dean, F. Mayor, T. P. McKenna, M. M. Fejer, and A. Safavi-Naeini, Single-mode squeezed-light generation and tomography with an integrated optical parametric oscillator, Sci. Adv. **10**, eadl1814 (2024).

[46] K. Goda, E. E. Mikhailov, O. Miyakawa, S. Saraf, S. Vass, A. Weinstein, and N. Mavalvala, Generation of a stable low-frequency squeezed vacuum field with periodically poled $KTiOPO_4$ at 1064 nm, Opt. Lett. **33**, 92 (2008).

[47] I. Krasnokutska, J.-L. J. Tambasco, X. Li, and A. Peruzzo, Ultra-low loss photonic circuits in lithium niobate on insulator, Opt. Express **26**, 897 (2018).

[48] D. Zhu, L. Shao, M. Yu, R. Cheng, B. Desiatov, C. J. Xin, Y. Hu, J. Holzgrafe, S. Ghosh, A. Shams-Ansari, E. Puma, N. Sinclair, C. Reimer, M. Zhang, and M. Lončar, Integrated photonics on thin-film lithium niobate, Adv. Opt. Photon. **13**, 242 (2021).

[49] M. Chen, C. Wang, X.-H. Tian, J. Tang, X. Gu, G. Qian, K. Jia, H.-Y. Liu, Z. Yan, Z. Ye, Z. Yin, S.-N. Zhu, and Z. Xie, Wafer-scale periodic poling of thin-film lithium niobate, Materials **17**, 1720 (2024).

[50] P.-K. Chen, I. Briggs, S. Hou, and L. Fan, Ultra-broadband quadrature squeezing with thin-film lithium niobate nanophotonics, Opt. Lett. **47**, 1506 (2022).

[51] D. Peace, A. Zappacosta, R. Cernansky, B. Haylock, A. Boes, A. Mitchell, and M. Lobino, Picosecond pulsed squeezing in thin-film lithium niobate strip-loaded waveguides at telecommunication wavelengths, J. Phys. Photon. **4**, 035002 (2022).

[52] K. Y. Spasibko, T. S. Iskhakov, and M. V. Chekhova, Spectral properties of high-gain parametric down-conversion, Opt. Express **20**, 7507 (2012).

[53] A. Christ, K. Laiho, A. Eckstein, K. N. Cassemiro, and C. Silberhorn, Probing multimode squeezing with correlation functions, New J. Phys. **13**, 033027 (2011).

[54] P. R. Sharapova, O. V. Tikhonova, S. Lemieux, R. W. Boyd, and M. V. Chekhova, Bright squeezed vacuum in a nonlinear interferometer: Frequency and temporal Schmidt-mode description, Phys. Rev. A **97**, 053827 (2018).

[55] T. S. Iskhakov, A. M. Pérez, K. Y. Spasibko, M. V. Chekhova, and G. Leuchs, Superbunched bright squeezed vacuum state, Opt. Lett. **37**, 1919 (2012).

[56] C. Wang, Z. Li, M.-H. Kim, X. Xiong, X.-F. Ren, G.-C. Guo, N. Yu, and M. Lončar, Metasurface-assisted phase-matching-free second harmonic generation in lithium niobate waveguides, Nat. Commun. **8**, 2098 (2017).

[57] B. Fang, H. Li, S. Zhu, and T. Li, Second-harmonic generation and manipulation in lithium niobate slab waveguides by grating metasurfaces, Photon. Res. **8**, 1296 (2020).

[58] N. Quesada, G. Triginer, M. D. Vidrighin, and J. E. Sipe, Theory of high-gain twin-beam generation in waveguides: From Maxwell's equations to efficient simulation, Phys. Rev. A **102**, 033519 (2020).

[59] M. Houde and N. Quesada, Waveguided sources of consistent, single-temporal-mode squeezed light: The good, the bad, and the ugly, AVS Quantum Sci. **5**, 011404 (2023).

[60] P.-H. Wang, S.-P. Wang, N.-L. Hou, Z.-R. Yang, W.-H. Huang, and T.-H. Lee, Flexible dispersion engineering using polymer patterning in nanophotonic waveguides, Sci. Rep. **13**, 13211 (2023).

[61] L. Cai, A. V. Gorbach, Y. Wang, A. Shams-Ansari, X. Ren, C. Langrock, B. Desiatov, T. A. Abebe, M. Povolotskyi, H. Efeoglu, J. E. Bowers, Y. Fainman, D. Englund, M. Lončar, S. Kumar, C. Gentry, A. Faraon, J. E. Sipe, X. Liu, A. Rabinovich, *et al.*, Highly efficient broadband second harmonic generation mediated by mode hybridization and nonlinearity patterning in compact fiber-integrated lithium niobate nano-waveguides, Sci. Rep. **8**, 12478 (2018).

[62] Z. Yang, M. Liscidini, and J. E. Sipe, Spontaneous parametric down-conversion in waveguides: A backward Heisenberg picture approach, Phys. Rev. A **77**, 033808 (2008).

[63] A. Christ, B. Brecht, W. Mauerer, and C. Silberhorn, Theory of quantum frequency conversion and type-II parametric down-conversion in the high-gain regime, New J. Phys. **15**, 053038 (2013).

[64] C. C. Gerry and P. L. Knight, *Introductory Quantum Optics* (Cambridge University Press, Cambridge, 2005).

[65] A. Krstić, F. Setzpfandt, and S. Saravi, Nonperturbative theory of spontaneous parametric down-conversion in open and dispersive optical systems, Phys. Rev. Res. **5**, 043228 (2023).

[66] P. T. Nam, M. Napiórkowski, and J. P. Solovej, Diagonalization of bosonic quadratic Hamiltonians by Bogoliubov transformations, J. Funct. Anal. **270**, 4340 (2016).

[67] L. G. Helt and N. Quesada, Degenerate squeezing in waveguides: A unified theoretical approach, J. Phys. Photon. **2**, 035001 (2020).

[68] C. Weedbrook, S. Pirandola, R. García-Patrón, N. J. Cerf, T. C. Ralph, J. H. Shapiro, and S. Lloyd, Gaussian quantum information, Rev. Mod. Phys. **84**, 621 (2012).

[69] C. K. Law, I. A. Walmsley, and J. H. Eberly, Continuous frequency entanglement: Effective finite Hilbert space and entropy control, Phys. Rev. Lett. **84**, 5304 (2000).

[70] T. E. Keller and M. H. Rubin, Theory of two-photon entanglement for spontaneous parametric down-conversion driven by a narrow pump pulse, Phys. Rev. A **56**, 1534 (1997).

[71] A. Christ, A. Eckstein, P. J. Mosley, and C. Silberhorn, Pure single photon generation by type-I PDC with backward-wave amplification, Opt. Express **17**, 3441 (2009).

[72] M. Jankowski, N. Jornod, C. Langrock, B. Desiatov, A. Marandi, M. Lončar, and M. M. Fejer, Quasi-static optical parametric amplification, Optica **9**, 273 (2022).

[73] D. S. Hum and M. M. Fejer, Quasi-phasematching, C. R. Phys. **8**, 180 (2007).

[74] F. Ayhan, M. Ludwig, T. Herr, V. Brasch, and L. G. Villanueva, Fabrication of periodically poled lithium niobate waveguides for broadband nonlinear photonics, APL Photon. **10**, 016118 (2025).

[75] J. Huang, X. P. Xie, C. Langrock, R. V. Roussev, D. S. Hum, and M. M. Fejer, Amplitude modulation and apodization of quasi-phase-matched interactions, Opt. Lett. **31**, 604 (2006).

[76] G. Thekkadath, M. Houde, D. England, P. Bustard, F. Bouchard, N. Quesada, and B. Sussman, Gain-induced group delay in spontaneous parametric down-conversion, Phys. Rev. Lett. **133**, 203601 (2024).

[77] N. Quesada and J. E. Sipe, Time-ordering effects in the generation of entangled photons using nonlinear optical processes, Phys. Rev. Lett. **114**, 093903 (2015).

[78] W. P. Grice, A. B. U'Ren, and I. A. Walmsley, Eliminating frequency and space-time correlations in multiphoton states, Phys. Rev. A **64**, 063815 (2001).

[79] P. J. Mosley, J. S. Lundeen, B. J. Smith, P. Wasylczyk, A. B. U'Ren, C. Silberhorn, and I. A. Walmsley, Heralded generation of ultrafast single photons in pure quantum states, Phys. Rev. Lett. **100**, 133601 (2008).

[80] V. Ansari, J. M. Donohue, B. Brecht, and C. Silberhorn, Tailoring nonlinear processes for quantum optics with pulsed temporal-mode encodings, Optica **5**, 534 (2018).

[81] P. Prudkovskii, Effective group velocity and shape of twin beams, JETP Lett. **111**, 428 (2020).

[82] A. B. U'Ren, C. Silberhorn, R. Erdmann, K. Banaszek, W. P. Grice, I. A. Walmsley, and M. G. Raymer, Generation of pure-state single-photon wavepackets by conditional preparation based on spontaneous parametric downconversion, Laser Phys. **15**, 146 (2005).

[83] J. Kumar, A. Krstić, S. Saravi, and F. Setzpfandt, Toward spectral engineering of squeezed light in high-gain parametric downconversion, Zenodo, 2026, https://zenodo.org/records/21456414.

[84] M. Fiorentino, S. M. Spillane, R. G. Beausoleil, T. D. Roberts, P. Battle, and M. W. Munro, Spontaneous parametric down-conversion in periodically poled KTP waveguides and bulk crystals, Opt. Express **15**, 7479 (2007).

[85] A. Martin, A. Issautier, H. Herrmann, W. Sohler, D. B. Ostrowsky, O. Alibart, and S. Tanzilli, A polarization entangled photon-pair source based on a type-II PPLN waveguide emitting at a telecom wavelength, New J. Phys. **12**, 103005 (2010).

[86] J. He, M. Lin, and F. Ma, Second harmonic generation in apodized chirped periodically poled lithium niobate loaded waveguides based on bound states in continuum, Photon. **11**, 769 (2024).

[87] J. Flórez, J. S. Lundeen, and M. V. Chekhova, Pump depletion in parametric down-conversion with low pump energies, Opt. Lett. **45**, 4264 (2020).

[88] G. P. Agrawal, *Nonlinear Fiber Optics*, 6th ed. (Academic, London, 2019).

[89] H. Li, F. Huang, J. Guo, H. Gao, H. Li, Z. Wu, X. Yao, Z. Bao, H. Li, Y. Shi, Z. Yu, and D. Dai, Pockels effect induced strong Kerr nonlinearity in a lithium niobate waveguide, Appl. Phys. Rev. **13**, 011428 (2026).

[90] Y. He, H. Liang, R. Luo, M. Li, and Q. Lin, Dispersion engineered high quality lithium niobate microring resonators, Opt. Express **26**, 16315 (2018).

[91] C. Wang, C. Langrock, A. Marandi, M. Jankowski, M. Zhang, B. Desiatov, M. M. Fejer, and M. Lončar, Ultrahigh-efficiency wavelength conversion in nanophotonic periodically poled lithium niobate waveguides, Optica **5**, 1438 (2018).

[92] M. Jankowski, C. Langrock, B. Desiatov, A. Marandi, C. Wang, M. Zhang, C. R. Phillips, M. Lončar, and M. M. Fejer, Ultrabroadband nonlinear optics in nanophotonic periodically poled lithium niobate waveguides, Optica **7**, 40 (2020).

[93] B. Taheri, D. Kopylov, M. Hammer, T. Meier, J. Förstner, and P. Sharapova, Gain-induced spectral non-degeneracy in type-II parametric down-conversion, arXiv:2603.01656.